

Entropy stable finite difference schemes for One-Fluid Two-Temperature Euler Non-equilibrium Hydrodynamics

Chetan Singh^{a,*}, Harish Kumar^{a,b}

^aDepartment of Mathematics, Indian Institute of Technology Delhi, India

^bIITD-Abu Dhabi, Abu Dhabi, UAE

ARTICLE INFO

Keywords:

One-fluid two-temperature Euler equations
Non-conservative hyperbolic system
Entropy stability
Finite-difference entropy stable schemes

ABSTRACT

In this work, we consider the One-Fluid Two-Temperature Euler (OFTT-Euler) equations used for modeling non-equilibrium hydrodynamics. The model comprises a system of nonlinear hyperbolic partial differential equations with non-conservative products. The model decomposed the total pressure into two scalar components: one for electrons and one for ions. Our aim in this work is to design entropy-stable finite difference numerical schemes for the model. This is achieved by reformulating the equations such that the reformulated non-conservative part does not contribute to the entropy. Then, we design higher-order entropy-conservative numerical schemes by using Tadmor's relation for the conservative part and higher-order central differences for the non-conservative parts. Finally, we design the entropy-dissipation terms using the entropy-scaled right eigenvectors of the conservative part, thereby deriving the entropy inequality for the entire system. We present several test cases in one and two dimensions to demonstrate the accuracy and stability of the proposed schemes.

1. Introduction

Radiation hydrodynamics plays an essential role in astrophysics [1, 2, 3, 4], inertial confinement fusion (ICF) [5, 6, 7, 8], and high energy density physics fields [9, 10, 11, 12]. The phenomenon models radiative, high-energy-density plasmas containing ions and electrons, with each species in its own thermal equilibrium. This results in each species (ions and electrons) having different temperatures, which are typically not equal; hence, they need to be evolved separately.

Assuming quasi-neutrality and ignoring radiative effects yields a fluid description with one density and velocity but two distinct temperatures. The model is known as the One-Fluid Two-Temperature Euler (OFTT-Euler) system. The model was proposed in [13], and ignores viscosity, thermal relaxation, and thermal conduction.

The model is a system of hyperbolic partial differential equations with non-conservative products. Hence, developing stable numerical methods is particularly challenging. The key difficulty is choosing a specific path to define weak admissible solutions, which is usually unknown [14]. Also, the numerical solutions are affected by the numerical viscosity [15]. Usually, a linear path is considered to design approximate Riemann solvers [13, 16, 17, 18, 19]. Numerical methods for the OFTT-Euler models have been developed in several articles [20, 21, 22, 23, 24, 25, 26, 27, 28, 29]. Also, for the related model, in [17, 16], authors have presented numerical schemes for the three-temperature radiation hydrodynamics equations, which govern the evolution of the interaction between radiation and plasmas. In [30], the authors presented simulations of two-material, two-temperature compressible flows. Additionally, in [31], the authors have developed a fifth-order equilibrium-preserving, path-conservative, characteristic-wise AWENO scheme for the OFTT-Euler model that incorporates electron-ion energy-exchange source terms. For the OFTT-Euler equations, in [13], a higher-order discontinuous Galerkin method is proposed. More recently, authors have proposed positivity-preserving higher-order discontinuous Galerkin methods for two-temperature compressible flows in [32].

As the OFTT-Euler system is hyperbolic, entropy stability is one of the few theoretical nonlinear stability estimates. Hence, it is desirable to design numerical methods that are consistent with the entropy condition associated with the system. Several authors have developed entropy-stable finite-difference schemes for hyperbolic systems in conservative form [33, 34, 35, 36, 37, 38, 39, 40]. More recently, these methods have been extended to several non-conservative

*Corresponding author.

✉ chetansingh9956@gmail.com (C. Singh); hkumar@iitd.ac.in (H. Kumar)
ORCID(s): 0009-0002-6822-8696 (C. Singh)

systems [41, 42, 43, 44]. In this paper, we propose entropy-stable finite difference schemes for the OFTT-Euler system. This is achieved as follows:

1. First, we present the entropy stability of the OFTT-Euler system at the continuous level. Then, following [42, 41], we propose the reformulation of the OFTT-Euler system such that the new non-conservative terms play no role in the entropy evolution.
2. For the new conservative part, we first derive the second-order entropy-conservative numerical flux, which is then used to design higher-order entropy-conservative numerical fluxes. Combining this with a suitable higher-order central difference-based discretization of the derivatives in non-conservative terms, we achieve entropy conservation for the whole system.
3. To achieve entropy stability, we then design a higher-order entropy diffusion operator using entropy-scaled eigenvectors for the conservative parts. The whole scheme is then shown to be entropy stable.

The rest of the article is organized as follows: In Section 2, we introduce the OFTT-Euler system and present its eigenvalues and eigenvectors. In Section 3, we first analyze the entropy framework of the OFTT-Euler system. We then present a novel reformulation of the OFTT-Euler equations, which makes the equations suitable for designing entropy stable schemes. In Section 4, we present the entropy stable finite-difference scheme for the reformulated OFTT-Euler model. Section 5 contains the time discretization. In Section 6, we present numerical test cases. Finally, Section 7 provides concluding remarks.

2. OFTT-Euler model for non-equilibrium Hydrodynamics

Following [13, 32], the OFTT-Euler model is given by,

$$\frac{\partial}{\partial t} \begin{pmatrix} \rho \\ \rho \mathbf{v} \\ \rho e_e \\ \rho e_i \end{pmatrix} + \nabla \cdot \begin{pmatrix} \rho \mathbf{v} \\ \rho \mathbf{v} \otimes \mathbf{v} + p \mathbf{I} \\ \rho e_e \mathbf{v} \\ \rho e_i \mathbf{v} \end{pmatrix} = \begin{pmatrix} 0 \\ \mathbf{0} \\ -p_e \nabla \cdot \mathbf{v} \\ -p_i \nabla \cdot \mathbf{v} \end{pmatrix}. \quad (1)$$

Here, ρ is the density, $\mathbf{v} = (v_x, v_y)^\top$ is the velocity, p is the total pressure of the fluid. The total fluid pressure p is described as $p = p_e + p_i$, where p_e and p_i are the pressures for electrons and ions, respectively. Similarly, e_e and e_i are the specific internal energies for electrons and ions, respectively. Following [13], we consider the ideal gas behavior for both species and use the following equation of state:

$$\rho e_e = C_{ve} \rho T_e = \frac{p_e}{\gamma_e - 1} \quad \text{and} \quad \rho e_i = C_{vi} \rho T_i = \frac{p_i}{\gamma_i - 1}. \quad (2)$$

Here, C_{ve} and C_{vi} denote the specific heats, and T_e and T_i are the temperatures for electrons and ions, respectively. The parameters γ_e and γ_i are the specific heat ratios for the species, with the constraints $C_{ve} > 0$, $C_{vi} > 0$, $\gamma_e > 1$, and $\gamma_i > 1$. We also define the total energy,

$$E = \rho e + \frac{\rho |\mathbf{v}|^2}{2} = \frac{p_e}{\gamma_e - 1} + \frac{p_i}{\gamma_i - 1} + \frac{\rho |\mathbf{v}|^2}{2} \quad (3)$$

where $e = e_e + e_i$ is the specific total internal energy of the fluid. The equations (1a) and (1b) are the conservation of mass and momentum, respectively. The other two equations are for the evolution of the internal energies for each species. We have highlighted the non-conservative terms in blue. Combining (1), (2) and (3), we obtain the conservation of total energy,

$$\frac{\partial E}{\partial t} + \nabla \cdot ((E + p) \mathbf{v}) = 0.$$

Replacing the electron internal energy equations (1c) with the total energy equation, the system (1) with conservative variables $\mathbf{U} = (\rho, \rho \mathbf{v}, E, p_i)^\top$, can be expressed as follows:

$$\frac{\partial}{\partial t} \begin{pmatrix} \rho \\ \rho \mathbf{v} \\ E \\ p_i \end{pmatrix} + \nabla \cdot \begin{pmatrix} \rho \mathbf{v} \\ \rho \mathbf{v} \otimes \mathbf{v} + p \mathbf{I} \\ ((E + p) \mathbf{v}) \\ p_i \mathbf{v} \end{pmatrix} = \begin{pmatrix} 0 \\ \mathbf{0} \\ 0 \\ -(\gamma_i - 1) p_i \nabla \cdot \mathbf{v} \end{pmatrix} \quad (4)$$

Again, we have highlighted the non-conservative terms in blue. The set of equations (1) can be written in quasilinear form,

$$\frac{\partial \mathbf{W}}{\partial t} + \mathcal{A}_x \frac{\partial \mathbf{W}}{\partial x} + \mathcal{A}_y \frac{\partial \mathbf{W}}{\partial y} = 0,$$

where, $\mathbf{W} = \{\rho, \mathbf{v}, p_e, p_i\}$ is the vector of primitive variables and the matrices \mathcal{A}_x and \mathcal{A}_y are given by,

$$\mathcal{A}_x = \begin{pmatrix} v_x & \rho & 0 & 0 & 0 \\ 0 & v_x & 0 & \frac{1}{\rho} & \frac{1}{\rho} \\ 0 & 0 & v_x & 0 & 0 \\ 0 & \gamma_e p_e & 0 & v_x & 0 \\ 0 & \gamma_i p_i & 0 & 0 & v_x \end{pmatrix}, \quad \text{and } \mathcal{A}_y = \begin{pmatrix} v_y & 0 & \rho & 0 & 0 \\ 0 & v_y & 0 & 0 & 0 \\ 0 & 0 & v_y & \frac{1}{\rho} & \frac{1}{\rho} \\ 0 & 0 & \gamma_e p_e & v_y & 0 \\ 0 & 0 & \gamma_i p_i & 0 & v_y \end{pmatrix}.$$

For the solutions to be physically admissible, we consider the solution set,

$$\Omega = \{\mathbf{U} \in \mathbb{R}^5 \mid \rho > 0, p_e > 0, p_i > 0\}. \quad (5)$$

For the states $\mathbf{U} \in \Omega$, the system (1) is hyperbolic and the eigenvalues of the OFTT-Euler system are,

$$\Lambda^d = (v_d, v_d, v_d, v_d \pm c_f), \quad c_f = \sqrt{\frac{(\gamma_e p_e + \gamma_i p_i)}{\rho}}, \quad d \in \{x, y\}. \quad (6)$$

The set of right eigenvectors of the matrix \mathcal{A}_x corresponding to eigenvalues v_x, v_x, v_x , and $v_x \pm c_f$ are

$$\mathcal{R}_{v_x}^1 = \begin{pmatrix} 1 \\ 0 \\ 0 \\ 0 \\ 0 \end{pmatrix}, \quad \mathcal{R}_{v_x}^2 = \begin{pmatrix} 0 \\ 0 \\ 1 \\ 0 \\ 0 \end{pmatrix}, \quad \mathcal{R}_{v_x}^3 = \begin{pmatrix} 0 \\ 0 \\ 0 \\ -1 \\ 1 \end{pmatrix}, \quad \text{and } \mathcal{R}_{v_x \pm c_f} = \begin{pmatrix} \frac{\rho^2}{\pm \sqrt{(\gamma_e p_e + \gamma_i p_i) \rho}} \\ 0 \\ \gamma_e p_e \rho \\ \gamma_i p_i \rho \end{pmatrix},$$

respectively. Similarly, the right eigenvectors of \mathcal{A}_y corresponding to eigenvalues $v_y, v_y, v_y, v_y \pm c_f$ are,

$$\mathcal{R}_{v_y}^1 = \begin{pmatrix} 1 \\ 0 \\ 0 \\ 0 \\ 0 \end{pmatrix}, \quad \mathcal{R}_{v_y}^2 = \begin{pmatrix} 0 \\ 1 \\ 0 \\ 0 \\ 0 \end{pmatrix}, \quad \mathcal{R}_{v_y}^3 = \begin{pmatrix} 0 \\ 0 \\ 0 \\ -1 \\ 1 \end{pmatrix}, \quad \text{and } \mathcal{R}_{v_y \pm c_f} = \begin{pmatrix} \frac{\rho^2}{\pm \sqrt{(\gamma_e p_e + \gamma_i p_i) \rho}} \\ 0 \\ \gamma_e p_e \rho \\ \gamma_i p_i \rho \end{pmatrix},$$

respectively. Now, we have the following result,

Lemma 2.1. *For the system (4), the characteristic fields corresponding to the eigenvalues u_d , $d \in \{x, y\}$ are linearly degenerate, and the characteristic fields corresponding to the eigenvalues $u_d \pm c_f$ are genuinely nonlinear.*

Proof. We will prove the result only in the x -direction. Proof for the y -direction is similar. For the eigenvalue v_x ,

$$\nabla v_x = \{0, 1, 0, 0, 0\}.$$

Now it's easy to see that,

$$\nabla v_x \cdot \mathcal{R}_{v_x}^i = 0, \quad i \in \{1, 2, 3\}.$$

For the eigenvalue $v_x \pm c_f$,

$$\nabla (v_x \pm c_f) = \left\{ \mp \frac{\sqrt{(p_e \gamma_e + p_i \gamma_i)}}{2\rho \sqrt{\rho}}, 1, 0, \pm \frac{\gamma_e}{2\sqrt{(p_e \gamma_e + p_i \gamma_i) \rho}}, \pm \frac{\gamma_i}{2\sqrt{(p_e \gamma_e + p_i \gamma_i) \rho}} \right\}.$$

A simple calculation shows that,

$$\nabla v_x \cdot \mathcal{R}_{v_x \pm c_f} = \pm \frac{(p_e \gamma_e (1 + \gamma_e) + p_i \gamma_i (1 + \gamma_i)) \rho}{2 \sqrt{(p_e \gamma_e + p_i \gamma_i) \rho}},$$

which clearly do not vanish for the admissible solutions. \square

3. Entropy analysis and reformulation

The entropy \mathcal{E} and the entropy flux \mathbf{q}_d for the OFTT-Euler system (4), are given by,

$$\mathcal{E} = -\rho s, \quad \mathbf{q}_d = -\rho v_d s, \quad s = \frac{1}{(\gamma_e - 1)} \ln \left(\frac{p_e}{\rho^{\gamma_e}} \right) + \frac{1}{(\gamma_i - 1)} \ln \left(\frac{p_i}{\rho^{\gamma_i}} \right), \quad (7)$$

where, $d \in \{x, y\}$. We now have the following result:

Lemma 3.1. *For a smooth solution of the OFTT-Euler system, we have the following equality,*

$$\partial_t s + v_x \partial_x s = 0,$$

which results in the entropy equality,

$$\partial_t \mathcal{E} + \partial_x \mathbf{q}_x = 0. \quad (8)$$

Proof. From system (1), we have,

$$\begin{aligned} \partial_t \rho + v_x \partial_x \rho + \rho \partial_x v_x &= 0, \\ \partial_t p_e + v_x \partial_x p_e + p_e \partial_x v_x + (\gamma_e - 1) p_e \partial_x v_x &= 0, \\ \partial_t p_i + v_x \partial_x p_i + p_i \partial_x v_x + (\gamma_i - 1) p_i \partial_x v_x &= 0. \end{aligned}$$

Using these, we get,

$$\begin{aligned} \partial_t s &= -\frac{1}{(\gamma_e - 1) p_e} \{v_x \partial_x p_e + p_e \partial_x v_x + (\gamma_e - 1) p_e \partial_x v_x\} \\ &\quad -\frac{1}{(\gamma_i - 1) p_i} \{v_x \partial_x p_i + p_i \partial_x v_x + (\gamma_i - 1) p_i \partial_x v_x\} \\ &\quad + \left(\frac{\gamma_e}{(\gamma_e - 1) \rho} + \frac{\gamma_i}{(\gamma_i - 1) \rho} \right) \{v_x \partial_x \rho + \rho \partial_x v_x\}, \end{aligned}$$

and

$$v_x \partial_x s = \frac{v_x \partial_x p_e}{(\gamma_e - 1) p_e} + \frac{v_x \partial_x p_i}{(\gamma_i - 1) p_i} - \left(\frac{\gamma_e v_x \partial_x \rho}{(\gamma_e - 1) \rho} + \frac{\gamma_i v_x \partial_x \rho}{(\gamma_i - 1) \rho} \right).$$

Adding them results in,

$$\partial_t s + v_x \partial_x s = 0$$

Combining this with mass conservation results in (8). \square

Remark 3.1. *In two dimensions, the above entropy equality (8) is,*

$$\partial_t \mathcal{E} + \partial_x \mathbf{q}_x + \partial_y \mathbf{q}_y = 0, \quad (9)$$

and for non-smooth solutions, we have the entropy inequality,

$$\partial_t \mathcal{E} + \partial_x \mathbf{q}_x + \partial_y \mathbf{q}_y \leq 0. \quad (10)$$

3.1. Reformulation of OFFT-Euler System

Following the ideas in [41, 42], we want to reformulate the OFFT-Euler equations in such a way that non-conservative terms do not contribute to the entropy. We propose the following reformulation of the OFFT-Euler system (4) as,

$$\frac{\partial}{\partial t} \begin{pmatrix} \rho \\ \rho \mathbf{v} \\ E \\ p_i \end{pmatrix} + \nabla \cdot \begin{pmatrix} \rho \mathbf{v} \\ \rho \mathbf{v} \otimes \mathbf{v} + 2p_e \mathbf{I} \\ (E + 2p_e) \mathbf{v} \\ p_i \mathbf{v} \end{pmatrix} = \begin{pmatrix} 0 \\ \nabla \cdot ((p_e - p_i) \mathbf{I}) \\ \nabla \cdot ((p_e - p_i) \mathbf{v}) \\ -(\gamma_i - 1)p_i \nabla \cdot \mathbf{v} \end{pmatrix}. \quad (11)$$

where we will treat blue colored terms as a non-conservative product. The resulting system of equations can be written as,

$$\frac{\partial \mathbf{U}}{\partial t} + \frac{\partial \mathbf{f}_x}{\partial x} + \frac{\partial \mathbf{f}_y}{\partial y} + \mathbf{C}_x(\mathbf{U}) \frac{\partial \mathbf{U}}{\partial x} + \mathbf{C}_y(\mathbf{U}) \frac{\partial \mathbf{U}}{\partial y} = 0. \quad (12)$$

where the flux functions \mathbf{f}_x and \mathbf{f}_y are,

$$\mathbf{f}_x = \begin{pmatrix} \rho v_x \\ \rho v_x^2 + 2p_e \\ \rho v_x v_y \\ (E + 2p_e) v_x \\ p_i v_x \end{pmatrix}, \quad \mathbf{f}_y = \begin{pmatrix} \rho v_y \\ \rho v_x v_y \\ \rho v_y^2 + 2p_e \\ (E + 2p_e) v_y \\ p_i v_y \end{pmatrix},$$

The matrices \mathbf{C}_x and \mathbf{C}_y are given by,

$$\mathbf{C}_x(\mathbf{U}) = \begin{pmatrix} 0 & 0 & 0 & 0 & 0 \\ -\frac{(\gamma_e-1)|\mathbf{v}|^2}{2} & (\gamma_e-1)v_x & (\gamma_e-1)v_y & -(\gamma_e-1) & \frac{\gamma_e-1}{\gamma_i-1} + 1 \\ 0 & 0 & 0 & 0 & 0 \\ -\left(\frac{(\gamma_e-1)|\mathbf{v}|^2}{2} + \frac{p_i-p_e}{\rho}\right)v_x & (\gamma_e-1)v_x^2 + \frac{p_i-p_e}{\rho} & (\gamma_e-1)v_x v_y & -(\gamma_e-1)v_x & \left(\frac{\gamma_e-1}{\gamma_i-1} + 1\right)v_x \\ -\frac{(\gamma_i-1)p_i v_x}{\rho} & \frac{(\gamma_i-1)p_i}{\rho} & 0 & 0 & 0 \end{pmatrix}$$

and

$$\mathbf{C}_y(\mathbf{U}) = \begin{pmatrix} 0 & 0 & 0 & 0 & 0 \\ 0 & 0 & 0 & 0 & 0 \\ -\frac{(\gamma_e-1)|\mathbf{v}|^2}{2} & (\gamma_e-1)v_x & (\gamma_e-1)v_y & -(\gamma_e-1) & \frac{\gamma_e-1}{\gamma_i-1} + 1 \\ -\left(\frac{(\gamma_e-1)|\mathbf{v}|^2}{2} + \frac{p_i-p_e}{\rho}\right)v_y & (\gamma_e-1)v_x v_y & (\gamma_e-1)v_y^2 + \frac{p_i-p_e}{\rho} & -(\gamma_e-1)v_y & \left(\frac{\gamma_e-1}{\gamma_i-1} + 1\right)v_y \\ -\frac{(\gamma_i-1)p_i v_y}{\rho} & 0 & \frac{(\gamma_i-1)p_i}{\rho} & 0 & 0 \end{pmatrix},$$

respectively. The entropy variable $\mathcal{V} = \frac{\partial \mathcal{E}}{\partial \mathbf{U}}$ for the OFFT-Euler system (4), is given by,

$$\mathcal{V} = \left(\frac{\gamma_e}{(\gamma_e-1)} + \frac{\gamma_i}{(\gamma_i-1)} - s - \frac{\beta_e |\mathbf{v}|^2}{2}, \beta_e \mathbf{v}, -\beta_e, \frac{\beta_e - \beta_i}{(\gamma_i-1)} \right)^\top, \quad (13)$$

where, $\beta_e = \frac{\rho}{p_e}$ and $\beta_i = \frac{\rho}{p_i}$. We note that similar to the case in [41, 42], the flux functions \mathbf{f}_d with $d \in \{x, y\}$, satisfy the condition,

$$\mathbf{q}_d'(\mathbf{U}) = \mathcal{V} \mathbf{f}_d'(\mathbf{U}), \quad (14)$$

and the non-conservative matrices $\mathbf{C}_d(\mathbf{U})$, $d \in \{x, y\}$ satisfy the condition,

$$\mathcal{V}^\top \mathbf{C}_d(\mathbf{U}) = 0. \quad (15)$$

The proof is provided in Appendix A.

Remark 3.2. In Appendix B, we discuss the symmetrizability of the OFTT-Euler system. We show that the complete system is not symmetrizable. However, if we only consider the conservative part, the system is indeed symmetrizable due to the presence of an entropy pair.

4. Semi-discrete numerical schemes

The reformulated OFTT-Euler equation (12) are suitable for designing entropy stable finite difference numerical schemes. We start by considering a uniform mesh of size $(\Delta x, \Delta y)$ with cell centers at the grid points, (x_i, y_j) , $0 \leq i \leq n_x$ and $0 \leq j \leq n_y$. The vertices of the cells are given by $(x_{i+\frac{1}{2}}, y_{j+\frac{1}{2}})$ with $x_{i+\frac{1}{2}} = \frac{x_i + x_{i+1}}{2}$ and $y_{j+\frac{1}{2}} = \frac{y_j + y_{j+1}}{2}$.

A semi-discrete finite difference numerical scheme for the system (12), can be written as,

$$\frac{d\mathbf{U}_{i,j}}{dt} = -\frac{\mathbf{f}_{x,i+\frac{1}{2},j} - \mathbf{f}_{x,i-\frac{1}{2},j}}{\Delta x} - \frac{\mathbf{f}_{y,i,j+\frac{1}{2}} - \mathbf{f}_{y,i,j-\frac{1}{2}}}{\Delta y} - \mathbf{C}_x(\mathbf{U}_{i,j}) \left(\frac{\partial \mathbf{U}}{\partial x} \right)_{i,j} - \mathbf{C}_y(\mathbf{U}_{i,j}) \left(\frac{\partial \mathbf{U}}{\partial y} \right)_{i,j}. \quad (16)$$

Here, the numerical fluxes $\mathbf{f}_{x,i+\frac{1}{2},j}$ and $\mathbf{f}_{y,i,j+\frac{1}{2}}$ are consistent with the continuous fluxes \mathbf{f}_x and \mathbf{f}_y , respectively. Additionally, $\left(\frac{\partial \mathbf{U}}{\partial x} \right)_{i,j}$ and $\left(\frac{\partial \mathbf{U}}{\partial y} \right)_{i,j}$ are discretized using central difference approximations of appropriate order. We begin by developing higher-order entropy conservative schemes for system (12).

4.1. Higher order entropy conservative schemes

For a grid function $a_{i,j}$, let us first introduce the following notation for the jumps

$$\llbracket (\cdot) \rrbracket_{i+\frac{1}{2},j} = (\cdot)_{i+1,j} - (\cdot)_{i,j}, \quad \llbracket (\cdot) \rrbracket_{i,j+\frac{1}{2}} = (\cdot)_{i,j+1} - (\cdot)_{i,j},$$

and averages

$$\overline{(\cdot)}_{i+\frac{1}{2},j} = \frac{(\cdot)_{i+1,j} + (\cdot)_{i,j}}{2}, \quad \overline{(\cdot)}_{i,j+\frac{1}{2}} = \frac{(\cdot)_{i,j+1} + (\cdot)_{i,j}}{2},$$

across the cell boundaries. For the conservative part, we recall that symmetric, consistent numerical fluxes $\tilde{\mathbf{f}}_{x,i+\frac{1}{2},j}$ and $\tilde{\mathbf{f}}_{y,i,j+\frac{1}{2}}$ satisfying

$$\llbracket \mathcal{V} \rrbracket_{i+\frac{1}{2},j} \cdot \tilde{\mathbf{f}}_{x,i+\frac{1}{2},j} = \llbracket \mathcal{F}_x \rrbracket_{i+\frac{1}{2},j}, \quad \llbracket \mathcal{V} \rrbracket_{i,j+\frac{1}{2}} \cdot \tilde{\mathbf{f}}_{y,i,j+\frac{1}{2}} = \llbracket \mathcal{F}_y \rrbracket_{i,j+\frac{1}{2}}. \quad (17)$$

are entropy conservative (see [45, 39]) and second-order accurate. Here,

$$\mathcal{F}_d = \mathcal{V} \cdot \mathbf{f}_d - \mathbf{q}_d = 2\rho u_d, \quad d \in \{x, y\}. \quad (18)$$

are *entropy potentials*. We will now derive the expressions for these numerical fluxes. For the simplicity of the notation, we will drop the grid notation by subscripts i and j and instead use subscripts l and r to represent left and right states, respectively. Then the jumps and averages of these states are denoted by,

$$\llbracket a \rrbracket = a_r - a_l \quad \text{and} \quad \bar{a} = \frac{a_r + a_l}{2},$$

for a scalar function a . Let us also denote the logarithmic average

$$a^{\ln} = \frac{\llbracket a \rrbracket}{\llbracket \ln a \rrbracket}.$$

We will now describe the derivation of the entropy conservative numerical flux $\tilde{\mathbf{f}}_x$ in x -direction, denoted componentwise as,

$$\tilde{\mathbf{f}}_x(\mathbf{U}_l, \mathbf{U}_r) = [\tilde{f}_x^{(1)}, \tilde{f}_x^{(2)}, \tilde{f}_x^{(3)}, \tilde{f}_x^{(4)}, \tilde{f}_x^{(5)}]^\top.$$

In [45, 39, 37, 46, 47], several authors have proposed different approaches for calculating an entropy-conservative flux. To derive the expression for the flux $\tilde{\mathbf{f}}_x$, we follow the procedure described in [37].

Our aim to construct an entropy conservative flux $\tilde{\mathbf{f}}_x$ that satisfied the identity

$$\llbracket \mathcal{V} \rrbracket \cdot \tilde{\mathbf{f}}_x = \llbracket \mathcal{F}_x \rrbracket. \quad (19)$$

We first change the expression for jump in $\llbracket \mathcal{V} \rrbracket$, to express it in jumps $\llbracket \rho \rrbracket$, $\llbracket v_x \rrbracket$, $\llbracket v_y \rrbracket$, $\llbracket \beta_e \rrbracket$, $\llbracket \beta_i \rrbracket$ as

$$\llbracket \mathcal{V} \rrbracket = \begin{pmatrix} \frac{2}{\rho^{\ln}} \llbracket \rho \rrbracket + \frac{1}{(\gamma_i-1)} \frac{\llbracket \beta_i \rrbracket}{\beta_i^{\ln}} - \bar{\beta}_e (\bar{v}_x \llbracket v_x \rrbracket + \bar{v}_y \llbracket v_y \rrbracket) + \left[\frac{1}{(\gamma_e-1)\beta_e^{\ln}} - \frac{\overline{|v|^2}}{2} \right] \llbracket \beta_e \rrbracket \\ \bar{\beta}_e \llbracket v_x \rrbracket + \bar{v}_x \llbracket \beta_e \rrbracket \\ \bar{\beta}_e \llbracket v_y \rrbracket + \bar{v}_y \llbracket \beta_e \rrbracket \\ -\llbracket \beta_e \rrbracket \\ \frac{\llbracket \beta_e \rrbracket - \llbracket \beta_i \rrbracket}{\gamma_i-1} \end{pmatrix}.$$

Then $\llbracket \mathcal{V} \rrbracket \cdot \tilde{\mathbf{f}}_x$ can be written as,

$$\begin{aligned} \llbracket \mathcal{V} \rrbracket \cdot \tilde{\mathbf{f}}_x &= \frac{2\tilde{f}_x^{(1)}}{\rho^{\ln}} \llbracket \rho \rrbracket + (-\bar{v}_x \bar{\beta}_e \tilde{f}_x^{(1)} + \bar{\beta}_e \tilde{f}_x^{(2)}) \llbracket v_x \rrbracket \\ &+ (-\bar{v}_y \bar{\beta}_e \tilde{f}_x^{(1)} + \bar{\beta}_e \tilde{f}_x^{(3)}) \llbracket v_y \rrbracket + \left(\frac{\tilde{f}_x^{(1)}}{(\gamma_i-1)\beta_i^{\ln}} - \frac{\tilde{f}_x^{(5)}}{(\gamma_i-1)} \right) \llbracket \beta_i \rrbracket \\ &+ \left[\left(\frac{1}{(\gamma_e-1)\beta_e^{\ln}} - \frac{\overline{|v|^2}}{2} \right) \tilde{f}_x^{(1)} + \bar{v}_x \tilde{f}_x^{(2)} + \bar{v}_y \tilde{f}_x^{(3)} - \tilde{f}_x^{(4)} + \frac{\tilde{f}_x^{(5)}}{(\gamma_i-1)} \right] \llbracket \beta_e \rrbracket. \end{aligned} \quad (20)$$

Also, the right hand side of (19), simplifies to,

$$\llbracket \mathcal{F}_x \rrbracket = \llbracket 2\rho v_x \rrbracket = 2\bar{v}_x \llbracket \rho \rrbracket + 2\bar{\rho} \llbracket v_x \rrbracket. \quad (21)$$

By equating to jumps $\llbracket \rho \rrbracket$, $\llbracket v_x \rrbracket$, $\llbracket v_y \rrbracket$, $\llbracket \beta_e \rrbracket$, and $\llbracket \beta_i \rrbracket$, in (20) and (21), we get,

$$\begin{aligned} \tilde{f}_x^{(1)} &= \rho^{\ln} \bar{v}_x, \quad \tilde{f}_x^{(2)} = \frac{2\bar{\rho}}{\bar{\beta}_e} + \bar{v}_x \tilde{f}_x^{(1)}, \quad \tilde{f}_x^{(3)} = \bar{v}_y \tilde{f}_x^{(1)}, \quad \tilde{f}_x^{(5)} = \frac{\tilde{f}_x^{(1)}}{\beta_i^{\ln}}, \\ \tilde{f}_x^{(4)} &= \left[\frac{1}{(\gamma_e-1)\beta_e^{\ln}} - \frac{\overline{|v|^2}}{2} \right] \tilde{f}_x^{(1)} + \bar{v}_x \tilde{f}_x^{(2)} + \bar{v}_y \tilde{f}_x^{(3)} + \frac{\tilde{f}_x^{(5)}}{\beta_i^{\ln}}. \end{aligned}$$

Similarly, we can derive the expression of entropy conservative numerical flux in y-direction $\tilde{\mathbf{f}}_y = [\tilde{f}_y^{(1)}, \tilde{f}_y^{(2)}, \tilde{f}_y^{(3)}, \tilde{f}_y^{(4)}, \tilde{f}_y^{(5)}]^T$, which results in,

$$\begin{aligned} \tilde{f}_y^{(1)} &= \rho^{\ln} \bar{v}_y, \quad \tilde{f}_y^{(2)} = \bar{v}_x \tilde{f}_y^{(1)}, \quad \tilde{f}_y^{(3)} = \frac{2\bar{\rho}}{\bar{\beta}_e} + \bar{v}_y \tilde{f}_y^{(1)}, \quad \tilde{f}_y^{(5)} = \frac{\tilde{f}_y^{(1)}}{\beta_i^{\ln}}, \\ \tilde{f}_y^{(4)} &= \left[\frac{1}{(\gamma_e-1)\beta_e^{\ln}} - \frac{\overline{|v|^2}}{2} \right] \tilde{f}_y^{(1)} + \bar{v}_x \tilde{f}_y^{(2)} + \bar{v}_y \tilde{f}_y^{(3)} + \frac{\tilde{f}_y^{(5)}}{\beta_i^{\ln}}. \end{aligned}$$

It is easy to check that the above numerical fluxes are consistent with the continuous fluxes, \mathbf{f}_x and \mathbf{f}_y .

Remark 4.1. The scheme (16) with fluxes $\tilde{\mathbf{f}}_{x,i+\frac{1}{2},j} = \tilde{\mathbf{f}}_x(\mathbf{U}_{i,j}, \mathbf{U}_{i+1,j})$ and $\tilde{\mathbf{f}}_{y,i,j+\frac{1}{2}} = \tilde{\mathbf{f}}_y(\mathbf{U}_{i,j}, \mathbf{U}_{i,j+1})$ together with the 2nd-order central difference approximation of $\left(\frac{\partial U}{\partial x}\right)_{i,j}$ and $\left(\frac{\partial U}{\partial y}\right)_{i,j}$, is 2nd-order accurate approximation of (12) and entropy conservative i.e.

$$\frac{d}{dt} \mathcal{E}(\mathbf{U}_{i,j}) + \frac{\tilde{\mathbf{q}}_{x,i+\frac{1}{2},j} - \tilde{\mathbf{q}}_{x,i-\frac{1}{2},j}}{\Delta x} + \frac{\tilde{\mathbf{q}}_{y,i,j+\frac{1}{2}} - \tilde{\mathbf{q}}_{y,i,j-\frac{1}{2}}}{\Delta y} = 0, \quad (22)$$

holds. Here, the entropy fluxes $\tilde{\mathbf{q}}_x$ and $\tilde{\mathbf{q}}_y$, are defined as

$$\tilde{\mathbf{q}}_{x,i+\frac{1}{2},j} = \tilde{\mathbf{V}}_{i+\frac{1}{2},j} \cdot \tilde{\mathbf{f}}_{x,i+\frac{1}{2},j} - \tilde{\mathbf{F}}_{x,i+\frac{1}{2},j} \quad \text{and} \quad \tilde{\mathbf{q}}_{y,i,j+\frac{1}{2}} = \tilde{\mathbf{V}}_{i,j+\frac{1}{2}} \cdot \tilde{\mathbf{f}}_{y,i,j+\frac{1}{2}} - \tilde{\mathbf{F}}_{y,i,j+\frac{1}{2}}$$

which are consistent with (7). The proof follows from the entropy conservation property of the numerical fluxes and (15).

Following [48], we can construct $2p^{\text{th}}$ -order accurate numerical fluxes using second-order fluxes with $p \in \mathbb{Z}^+$. For $p = 2$, the 4^{th} -order entropy-conservative fluxes $\tilde{\mathbf{f}}_{x,i+\frac{1}{2},j}^4$ and $\tilde{\mathbf{f}}_{y,i,j+\frac{1}{2}}^4$ are given as follows:

$$\tilde{\mathbf{f}}_{x,i+\frac{1}{2},j}^4 = \frac{4}{3} \tilde{\mathbf{f}}_x(\mathbf{U}_{i,j}, \mathbf{U}_{i+1,j}) - \frac{1}{6} \left(\tilde{\mathbf{f}}_x(\mathbf{U}_{i-1,j}, \mathbf{U}_{i+1,j}) + \tilde{\mathbf{f}}_x(\mathbf{U}_{i,j}, \mathbf{U}_{i+2,j}) \right) \quad (23)$$

and

$$\tilde{\mathbf{f}}_{y,i,j+\frac{1}{2}}^4 = \frac{4}{3} \tilde{\mathbf{f}}_y(\mathbf{U}_{i,j}, \mathbf{U}_{i,j+1}) - \frac{1}{6} \left(\tilde{\mathbf{f}}_y(\mathbf{U}_{i,j-1}, \mathbf{U}_{i,j+1}) + \tilde{\mathbf{f}}_y(\mathbf{U}_{i,j}, \mathbf{U}_{i,j+2}) \right). \quad (24)$$

Remark 4.2. By replacing the 2^{nd} -order fluxes with the 4^{th} -order fluxes and using 4^{th} -order central difference approximations to approximate $\left(\frac{\partial U}{\partial x}\right)_{i,j}$ and $\left(\frac{\partial U}{\partial y}\right)_{i,j}$, the scheme (16) is 4^{th} -order entropy-conservative schemes i.e.

$$\frac{d}{dt} \mathcal{E}(\mathbf{U}_{i,j}) + \frac{\tilde{\mathbf{q}}_{x,i+\frac{1}{2},j}^4 - \tilde{\mathbf{q}}_{x,i-\frac{1}{2},j}^4}{\Delta x} + \frac{\tilde{\mathbf{q}}_{y,i,j+\frac{1}{2}}^4 - \tilde{\mathbf{q}}_{y,i,j-\frac{1}{2}}^4}{\Delta y} = 0, \quad (25)$$

holds. Here, the numerical entropy fluxes $\tilde{\mathbf{q}}_x^4$ and $\tilde{\mathbf{q}}_y^4$ are which are consistent with entropy fluxes (7).

4.2. Higher-order entropy-stable schemes

The schemes defined in Section 4.1 are designed to conserve entropy. However, in the presence of the discontinuities, it is necessary to have appropriate entropy decay; otherwise, the numerical solution will contain undesirable numerical oscillations. Following [39], we modify the numerical flux to include dissipation terms as,

$$\hat{\mathbf{f}}_{x,i+\frac{1}{2},j} = \tilde{\mathbf{f}}_{x,i+\frac{1}{2},j} - \frac{1}{2} \mathbf{D}_{x,i+\frac{1}{2},j} \llbracket \mathcal{V} \rrbracket_{i+\frac{1}{2},j}, \quad \hat{\mathbf{f}}_{y,i,j+\frac{1}{2}} = \tilde{\mathbf{f}}_{y,i,j+\frac{1}{2}} - \frac{1}{2} \mathbf{D}_{y,i,j+\frac{1}{2}} \llbracket \mathcal{V} \rrbracket_{i,j+\frac{1}{2}}. \quad (26)$$

The diffusion matrices $\mathbf{D}_{x,i+\frac{1}{2},j}$ and $\mathbf{D}_{y,i,j+\frac{1}{2}}$ are symmetric positive definite and are based on Rusanov's type diffusion operators, given by,

$$\mathbf{D}_{x,i+\frac{1}{2},j} = \tilde{\mathbf{R}}_{x,i+\frac{1}{2},j} \Lambda_{x,i+\frac{1}{2},j} \tilde{\mathbf{R}}_{x,i+\frac{1}{2},j}^{\top} \quad \text{and} \quad \mathbf{D}_{y,i,j+\frac{1}{2}} = \tilde{\mathbf{R}}_{y,i,j+\frac{1}{2}} \Lambda_{y,i,j+\frac{1}{2}} \tilde{\mathbf{R}}_{y,i,j+\frac{1}{2}}^{\top}. \quad (27)$$

Here, $\tilde{\mathbf{R}}_d$, $d \in \{x, y\}$ are the matrices of entropy-scaled right eigenvectors (see [49]) presented in Appendix C. Also, the matrices are Λ_d are diagonal matrices, given by,

$$\Lambda_d = \left(\max_{\lambda \in \tilde{\Lambda}_d} |\lambda| \right) \mathbf{I}_{5 \times 5},$$

where, $\tilde{\Lambda}_d$ is the set of eigenvalues of the flux Jacobian $\frac{\partial \mathbf{f}_d}{\partial \mathbf{U}}$ given in Appendix C.

Thus, the numerical scheme (16) with the modified flux (26) is entropy stable. However, the first-order jump terms $\llbracket \mathcal{V} \rrbracket_{i+\frac{1}{2},j}$ and $\llbracket \mathcal{V} \rrbracket_{i,j+\frac{1}{2}}$ restricts the overall accuracy to first order. Replacing these jumps with higher-order polynomial reconstructions improves accuracy but does not guarantee entropy stability. To address this issue, we follow the approach proposed in [38] and describe the process in x -direction. Same process is followed for reconstruction in y -direction. Let us introduce *scaled entropy variables*

$$\mathcal{W}_{x,i,j}^{\pm} = \tilde{\mathbf{R}}_{x,i \pm \frac{1}{2},j}^{\top} \mathcal{V}_{i,j}.$$

Using ENO reconstruction procedure, we reconstruct $\mathcal{W}_{x,i,j}^\pm$ with the k^{th} -degree polynomials $\mathcal{P}_{x,i,j}^\pm(x)$ and define,

$$\hat{\mathcal{W}}_{x,i,j}^\pm = \mathcal{P}_{x,i,j}^\pm(x_{i\pm\frac{1}{2}}).$$

Using these values, the reconstructed $[\![\mathcal{V}]\!]_{i+\frac{1}{2},j}$ of k -th order is defined as,

$$[\![\hat{\mathcal{V}}]\!]_{x,i,j}^k = \hat{\mathcal{V}}_{x,i+1,j}^- - \hat{\mathcal{V}}_{x,i,j}^+$$

where

$$\hat{\mathcal{V}}_{x,i+\frac{1}{2},j}^\pm = \left\{ \tilde{\mathbf{R}}_{x,i\pm\frac{1}{2},j}^\top \right\}^{(-1)} \hat{\mathcal{W}}_{x,i,j}^\pm.$$

Following [38], we define the higher-order entropy stable numerical flux in the x -direction as follows:

$$\hat{\mathbf{f}}_{x,i+\frac{1}{2},j}^k = \tilde{\mathbf{f}}_{x,i+\frac{1}{2},j}^{2p} - \frac{1}{2} \mathbf{D}_{x,i+\frac{1}{2},j} [\![\hat{\mathcal{V}}]\!]_{x,i+\frac{1}{2},j}^k, \quad (28)$$

where, k denotes the order of the scheme and $p \in \mathbb{N}$ is given by

$$p = \begin{cases} \frac{k}{2}, & \text{if } k \text{ is even,} \\ \frac{k+1}{2}, & \text{if } k \text{ is odd.} \end{cases}$$

To ensure the entropy stability of the modified flux, the reconstruction procedure for \mathcal{W} must satisfy the sign-preserving property, which is a sufficient condition for ensuring that the numerical flux (28) is entropy-stable. For the 2^{nd} -order scheme, the MinMod reconstruction is used to ensure this property. For higher-order schemes i.e. 3^{rd} -order ($k = 3$) and 4^{th} -order ($k = 4$) schemes, we employ ENO-based reconstruction [50], which ensures *sign-preserving property* of the reconstruction procedure. Following the same procedure in y -direction, we can define a higher numerical flux in the y -direction as follows:

$$\hat{\mathbf{f}}_{y,i,j+\frac{1}{2}}^k = \tilde{\mathbf{f}}_{y,i,j+\frac{1}{2}}^{2p} - \frac{1}{2} \mathbf{D}_{y,i,j+\frac{1}{2}} [\![\hat{\mathcal{V}}]\!]_{y,i,j+\frac{1}{2}}^k. \quad (29)$$

Now we have the following result:

Theorem 4.1. *The semi-discrete scheme (16) with entropy stable fluxes (28), (29) and with 2^{nd} -order (for $k = 2$) and 4^{th} -order (for $k = 3, 4$) central difference approximations to approximate $\left(\frac{\partial \mathbf{U}}{\partial x}\right)_{i,j}$ and $\left(\frac{\partial \mathbf{U}}{\partial y}\right)_{i,j}$, is k^{th} -order accurate and entropy stable, i.e. it satisfies,*

$$\frac{d}{dt} \mathcal{E}(U_{i,j}) + \frac{1}{\Delta x} \left(\hat{\mathbf{q}}_{x,i+\frac{1}{2},j}^k - \hat{\mathbf{q}}_{x,i-\frac{1}{2},j}^k \right) + \frac{1}{\Delta y} \left(\hat{\mathbf{q}}_{y,i,j+\frac{1}{2}}^k - \hat{\mathbf{q}}_{y,i,j-\frac{1}{2}}^k \right) \leq 0, \quad (30)$$

where $\hat{\mathbf{q}}_x^k$ and $\hat{\mathbf{q}}_y^k$ are given by,

$$\hat{\mathbf{q}}_{x,i+\frac{1}{2},j}^k = \tilde{\mathbf{q}}_{x,i+\frac{1}{2},j}^{2p} - \frac{1}{2} \tilde{\mathbf{v}}_{i+\frac{1}{2},j}^\top \mathbf{D}_{x,i+\frac{1}{2},j} [\![\hat{\mathcal{V}}]\!]_{x,i+\frac{1}{2},j}^k$$

and

$$\hat{\mathbf{q}}_{y,i,j+\frac{1}{2}}^k = \tilde{\mathbf{q}}_{y,i,j+\frac{1}{2}}^{2p} - \frac{1}{2} \tilde{\mathbf{v}}_{i,j+\frac{1}{2}}^\top \mathbf{D}_{y,i,j+\frac{1}{2}} [\![\hat{\mathcal{V}}]\!]_{y,i,j+\frac{1}{2}}^k.$$

are consistent numerical entropy fluxes with continuous entropy fluxes \mathbf{q}_x and \mathbf{q}_y , respectively.

Order	μ_{kl}			ν_{kl}		
2	1			1		
	1/2	1/2		0	1/2	
3	1			1		
	3/4	1/4		0	1/4	
	1/3	0	2/3	0	0	2/3

Table 1
Coefficients for explicit SSP-Runge-Kutta schemes

5. Fully discrete schemes

The semi-discrete scheme (16) can be expressed as follows:

$$\frac{d}{dt} \mathbf{U}_{i,j}(t) = \mathcal{L}_{i,j}(\mathbf{U}(t)) \quad (31)$$

where,

$$\mathcal{L}_{i,j}(\mathbf{U}(t)) = -\frac{f_{x,i+\frac{1}{2},j} - f_{x,i-\frac{1}{2},j}}{\Delta x} - \frac{f_{y,i,j+\frac{1}{2}} - f_{y,i,j-\frac{1}{2}}}{\Delta y} - \mathbf{C}_x(\mathbf{U}_{i,j}) \left(\frac{\partial \mathbf{U}}{\partial x} \right)_{i,j} - \mathbf{C}_y(\mathbf{U}_{i,j}) \left(\frac{\partial \mathbf{U}}{\partial y} \right)_{i,j}$$

Here \mathbf{U} is a grid function. Following [51], we use explicit strong stability-preserving Runge-Kutta (SSP-RK) methods for the time discretizations. Let $\mathbf{U}_{i,j}^n$ be the solution at time level t^n , with time step $\Delta t = t^{n+1} - t^n$. Then to update the solutions by one time step, the 2nd and 3rd-order accurate SSP-RK schemes are given as follows:

1. Set $\mathbf{U}_{i,j}^0 = \mathbf{U}_{i,j}^n$.
2. Compute

$$\mathbf{U}_{i,j}^{(k)} = \sum_{l=0}^{k-1} \mu_{kl} \mathbf{U}_{i,j}^{(l)} + \nu_{kl} \Delta t (\mathcal{L}_{i,j}(\mathbf{U}^{(l)})), \quad \text{For } k \in \{1, \dots, m+1\}$$

where μ_{kl} and ν_{kl} are given in Table (1).

3. Finally, $\mathbf{U}_{i,j}^{n+1} = \mathbf{U}_{i,j}^{(m+1)}$.

The 4th-order SSP-RK scheme [51] is given by,

$$\begin{aligned} \mathbf{U}^{(1)} &= \mathbf{U}^n + 0.39175222700392\Delta t (\mathcal{L}(\mathbf{U}^n)) \\ \mathbf{U}^{(2)} &= 0.44437049406734\mathbf{U}^n + 0.55562950593266\mathbf{U}^{(1)} + 0.36841059262959\Delta t (\mathcal{L}(\mathbf{U}^{(1)})) \\ \mathbf{U}^{(3)} &= 0.62010185138540\mathbf{U}^n + 0.37989814861460\mathbf{U}^{(2)} + 0.25189177424738\Delta t (\mathcal{L}(\mathbf{U}^{(2)})) \\ \mathbf{U}^{(4)} &= 0.17807995410773\mathbf{U}^n + 0.82192004589227\mathbf{U}^{(3)} + 0.54497475021237\Delta t (\mathcal{L}(\mathbf{U}^{(3)})) \\ \mathbf{U}^{n+1} &= 0.00683325884039\mathbf{U}^n + 0.51723167208978\mathbf{U}^{(2)} + 0.12759831133288\mathbf{U}^{(3)} \\ &\quad + 0.34833675773694\mathbf{U}^{(4)} + 0.08460416338212\Delta t (\mathcal{L}(\mathbf{U}^{(3)})) + 0.22600748319395\Delta t (\mathcal{L}(\mathbf{U}^{(4)})). \end{aligned}$$

Here, we have ignored the subscript for each cell for simplicity. Using the time discretizations, we now denote the compatible discretizations as follows:

6. Numerical Results

To calculate the time step, we use

$$\Delta t = \text{CFL} \frac{1}{\max_{i,j} \left(\frac{\lambda_x(\mathbf{U}_{i,j})}{\Delta x} + \frac{\lambda_y(\mathbf{U}_{i,j})}{\Delta y} \right)},$$

Scheme	Entropy Stable Scheme	$\left(\frac{\partial U}{\partial x}\right)_{i,j}$ and $\left(\frac{\partial U}{\partial y}\right)_{i,j}$ Approx.	Time Integration
$\mathbf{O2}_{\text{exp}}^{\text{es}}$	2 nd -order	2 nd -order central difference	SSP-RK2
$\mathbf{O3}_{\text{exp}}^{\text{es}}$	3 rd -order	4 th -order central difference	SSP-RK3
$\mathbf{O4}_{\text{exp}}^{\text{es}}$	4 th -order	4 th -order central difference	SSP-RK4

Table 2

Description of fully discrete numerical schemes

Table 3

 One-dimensional accuracy test-I: L_1 errors and order of accuracy for ρ .

Number of cells	$\mathbf{O2}_{\text{exp}}^{\text{es}}$		$\mathbf{O3}_{\text{exp}}^{\text{es}}$		$\mathbf{O4}_{\text{exp}}^{\text{es}}$	
	L_1 error	Order	L_1 error	Order	L_1 error	Order
20	1.57E-02	–	6.01E-03	–	1.49E-03	–
40	6.78E-03	1.209554054	7.65E-04	2.973502425	1.22E-04	3.615641272
80	2.02E-03	1.751322546	9.60E-05	2.994715944	8.80E-06	3.792707546
160	5.59E-04	1.849905978	1.20E-05	2.998908566	6.07E-07	3.85875165
320	1.53E-04	1.87285767	1.50E-06	2.99964837	4.11E-08	3.882974064
640	4.08E-05	1.902504771	1.88E-07	2.999930068	2.73E-09	3.910359146

where,

$$\lambda_d(\mathbf{U}_{i,j}) = \max_{\lambda \in \Lambda_d} |\lambda(\mathbf{U}_{i,j})|, \quad d \in \{x, y\}$$

are the absolute values of the maximum eigenvalues in each direction. For one-dimensional test cases, we take $\text{CFL} = 0.475$ for all schemes. For two-dimensional test cases, we take $\text{CFL} = 0.3$ for all schemes. To measure the total entropy production at every time step, we also compute the total entropy decay at each time step given by,

$$\sum_{i,j} \left[\mathcal{E}^{n+1}(\mathbf{U}_{i,j}) - \mathcal{E}^n(\mathbf{U}_{i,j}) - \frac{\Delta t}{\Delta x} \left(\hat{\mathbf{q}}_{x,i+\frac{1}{2},j}^k - \hat{\mathbf{q}}_{x,i-\frac{1}{2},j}^k \right) - \frac{\Delta t}{\Delta y} \left(\hat{\mathbf{q}}_{y,i,j+\frac{1}{2}}^k - \hat{\mathbf{q}}_{y,i,j-\frac{1}{2}}^k \right) \right]. \quad (33)$$

This will test the consistency of the numerical results with (30). We will now present the one and two-dimensional test cases.

6.1. One-dimensional accuracy test-I

To verify the accuracy and convergence rate of the proposed numerical schemes, we consider a smooth problem defined in [52], which is essentially a scalar problem and has only one non-trivial component, namely ρ . The initial conditions are,

$$\begin{aligned} \rho(x, 0) &= 1 + 0.2 \sin(x), \\ (\mathbf{v}, p_e, p_i) &= (1, 0, 2, 2), \end{aligned}$$

with $\gamma_e = \gamma_i = 1.4$. We consider the computational domain $[0, 2\pi]$ and use periodic boundary conditions. The exact solution for the problem is $\rho(x, t) = 1 + 0.2 \sin(x - t)$.

In Table(3), we have presented the L_1 -errors for density using the $\mathbf{O2}_{\text{exp}}^{\text{es}}$, $\mathbf{O3}_{\text{exp}}^{\text{es}}$ and $\mathbf{O4}_{\text{exp}}^{\text{es}}$ schemes at the final time of $t = 1.3$. We observe that all the schemes have achieved the theoretically predicted order of accuracy.

6.2. One-dimensional accuracy test-II

In this test case from [31], we consider the computational domain of $[0, 2]$, with periodic boundary conditions. The initial conditions are given by,

$$(\rho, \mathbf{v}, p_e, p_i) = (1 + 0.1 \sin \pi x, 1, 0, 0.6 + 0.1 \sin \pi x, 0.4 - 0.1 \sin \pi x).$$

with $\gamma_e = \gamma_i = \frac{5}{3}$.

Table 4

One-dimensional accuracy test-II: L_1 -errors and order of accuracy for p_e and p_i .

L_1 -errors and order of accuracy for p_e						
Number of cells	$\mathbf{O2}_{\text{exp}}^{\text{es}}$		$\mathbf{O3}_{\text{exp}}^{\text{es}}$		$\mathbf{O4}_{\text{exp}}^{\text{es}}$	
	L_1 -error	Order	L_1 -error	Order	L_1 -error	Order
40	5.16E-03	–	1.33E-04	–	2.44E-05	–
80	1.71E-03	1.592660617	1.66E-05	2.997894069	1.86E-06	3.711973538
160	4.75E-04	1.848363303	2.07E-06	2.999790989	1.31E-07	3.830772838
320	1.29E-04	1.884148797	2.59E-07	3.000067743	9.05E-09	3.852261967
640	3.48E-05	1.888114719	3.24E-08	3.000102719	6.22E-10	3.863408653

L_1 -errors and order of accuracy for p_i						
Number of cells	$\mathbf{O2}_{\text{exp}}^{\text{es}}$		$\mathbf{O3}_{\text{exp}}^{\text{es}}$		$\mathbf{O4}_{\text{exp}}^{\text{es}}$	
	L_1 -error	Order	L_1 -error	Order	L_1 -error	Order
40	5.13E-03	–	1.41E-04	–	2.46E-05	–
80	1.72E-03	1.574981354	1.78E-05	2.98947927	1.86E-06	3.7199136
160	4.77E-04	1.851188296	2.22E-06	2.997912249	1.32E-07	3.824447721
320	1.29E-04	1.882149615	2.78E-07	2.999345868	9.10E-09	3.853476906
640	3.49E-05	1.88953533	3.48E-08	2.999805725	6.24E-10	3.865837857

In Table(4), we have presented the L_1 -errors of electron and ion pressures, p_e and p_i , respectively, at the final simulation time $t = 1.0$, using different numerical schemes. Again, we observe that all the schemes have achieved the desired order of accuracy.

6.3. Double rarefaction Riemann problem

In this test case, we consider first one-dimensional Riemann problem from [13], where solution is consist of two rarefaction waves. We consider the computational domain of $[-5, 5]$ with Neumann boundary conditions. The initial states are separated by a discontinuity at $x = 0$ and are given as follows:

$$(\rho, \mathbf{v}, p_e, p_i) = \begin{cases} (2, -1, 0, 0.6, 0.4), & \text{if } x \leq 0 \\ (2, 1, 0, 0.4, 0.6), & \text{otherwise,} \end{cases}$$

with $\gamma_e = 1.4$ and $\gamma_i = 1.67$. We compute the solutions using 2000 cells till the final simulation time of $t = 2.0$.

Numerical results for the $\mathbf{O2}_{\text{exp}}^{\text{es}}$, $\mathbf{O3}_{\text{exp}}^{\text{es}}$ and $\mathbf{O4}_{\text{exp}}^{\text{es}}$ schemes are presented in Figure (1). We have plotted density, electron, and ion pressures and total entropy decay at each time step. We observe that all the waves are resolved. Also, we note that the second order scheme $\mathbf{O2}_{\text{exp}}^{\text{es}}$ more diffusive than the third ($\mathbf{O3}_{\text{exp}}^{\text{es}}$) and fourth ($\mathbf{O4}_{\text{exp}}^{\text{es}}$) order schemes. The results are similar to those presented in [13]. In Figure (1(d)), we have plotted the total entropy change (see (33)) at every time step. We observe that due the presence of an initial discontinuity, we have large entropy decay initially. However, after that, the entropy decay is almost negligible as no new waves are generated.

6.4. Sod Riemann problem

In this test from [13], we again consider a Riemann problem on the computational domain of $[-5, 5]$, with Neumann boundary conditions. The initial conditions are given by,

$$(\rho, \mathbf{v}, p_e, p_i) = \begin{cases} (1, 0, 0, 0.4, 0.6), & \text{if } x \leq 0 \\ (0.125, 0, 0, 0.06, 0.04), & \text{otherwise} \end{cases}$$

with $\gamma_e = \gamma_i = 1.4$. We use 2000 cells and compute till the final time $t = 2.0$.

We have presented numerical results in Fig.(2) for the $\mathbf{O2}_{\text{exp}}^{\text{es}}$, $\mathbf{O3}_{\text{exp}}^{\text{es}}$ and $\mathbf{O4}_{\text{exp}}^{\text{es}}$ schemes at time $t = 2.0$ using 2000 cells. We have plotted density, electron pressure, ion pressure and total entropy change with time. We observe that all the schemes are able to resolve the shocks, contact and rarefaction waves efficiently. We do see small oscillations in the second-order scheme $\mathbf{O2}_{\text{exp}}^{\text{es}}$ but they are stable in the sense that they do not increase with refinement. Furthermore, higher order schemes $\mathbf{O3}_{\text{exp}}^{\text{es}}$ and $\mathbf{O4}_{\text{exp}}^{\text{es}}$ do not have any oscillations. In addition, from the entropy decay plot we see that all the schemes are entropy stable and continue to have some entropy decay due to the presence of a shock in the solution. We also observe that $\mathbf{O2}_{\text{exp}}^{\text{es}}$ is slightly more diffusive than the $\mathbf{O3}_{\text{exp}}^{\text{es}}$ and $\mathbf{O4}_{\text{exp}}^{\text{es}}$ schemes.

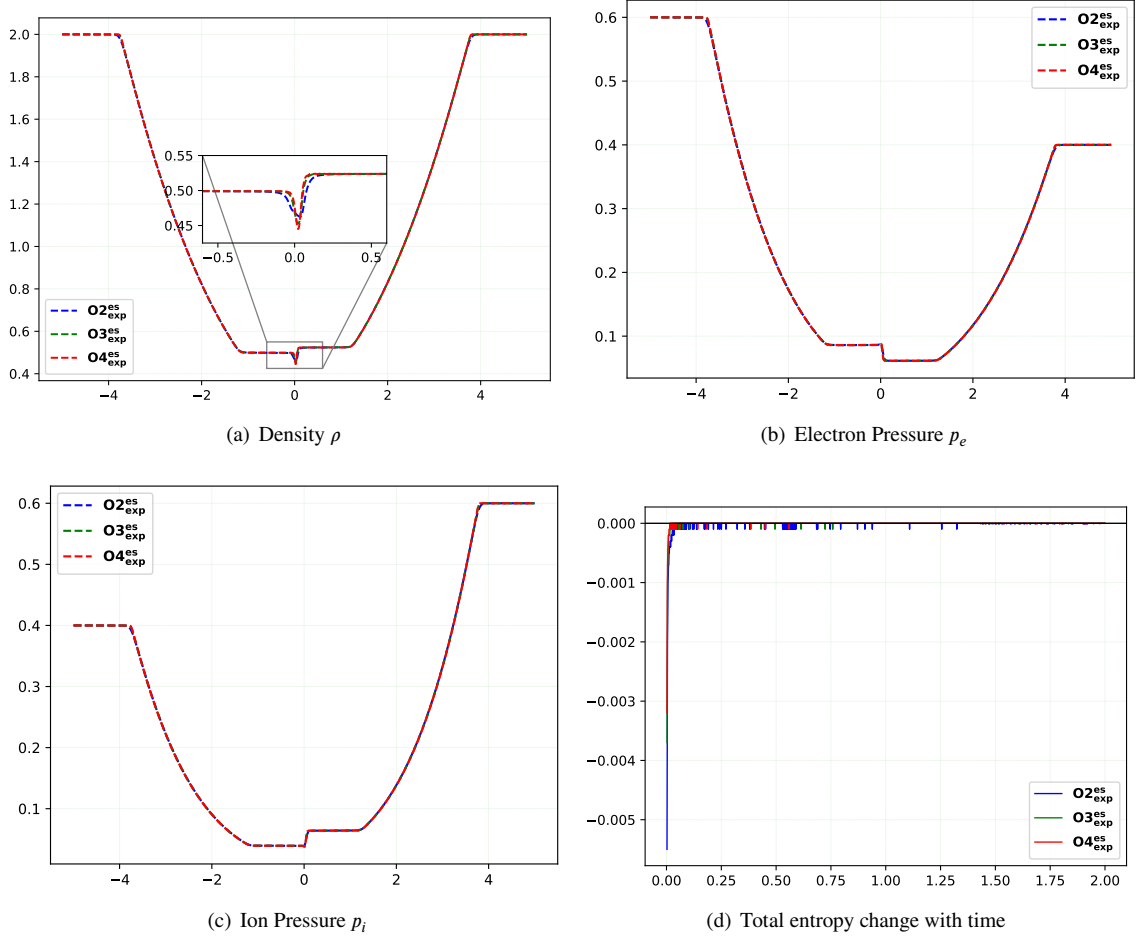


Figure 1: Double rarefaction Riemann problem: Plots of density, electron pressure, and ion pressure at $t = 2.0$ using 2000 cells. We have also plotted total entropy change with time.

6.5. Lax Riemann problem

In another test case from [13], we consider a Riemann problem on the computational domain of $[-5, 5]$ with Neumann boundary conditions. The initial conditions are given by,

$$(\rho, \mathbf{v}, p_e, p_i) = \begin{cases} (0.445, 0.689, 0, 1.764, 1.764), & \text{if } x \leq 0, \\ (0.5, 0, 0, 0.2855, 0.2855), & \text{otherwise,} \end{cases}$$

with $\gamma_e = 1.4$ and $\gamma_i = 1.67$. We have presented numerical results in Fig.(3) for the $\mathbf{O2}_{\text{exp}}^{\text{es}}$, $\mathbf{O3}_{\text{exp}}^{\text{es}}$, and $\mathbf{O4}_{\text{exp}}^{\text{es}}$ schemes at the final time of $t = 1.4$ on 2000 cells. The density, electron pressure, ion pressure, and change in total entropy with time are plotted in Figures (3(a)), (3(b)), (3(c)) and (3(d)), respectively. We again see that all the waves are resolved and $\mathbf{O2}_{\text{exp}}^{\text{es}}$ being most diffusive. We also observe small oscillations with $\mathbf{O2}_{\text{exp}}^{\text{es}}$ but they are stable with respect to refinement. We do not observe any oscillations in $\mathbf{O3}_{\text{exp}}^{\text{es}}$ and $\mathbf{O4}_{\text{exp}}^{\text{es}}$ schemes. In Figure (3(d)), we note that total entropy decays at every time step. We also see that total entropy decay is almost constant after initial changes. Furthermore, $\mathbf{O2}_{\text{exp}}^{\text{es}}$ decays more entropy when compared with $\mathbf{O3}_{\text{exp}}^{\text{es}}$ and $\mathbf{O4}_{\text{exp}}^{\text{es}}$.

6.6. Two-dimensional accuracy test

To verify the accuracy and convergence rate of our numerical schemes, we consider a smooth problem defined in [52], which is essentially a scalar problem and has only one non-trivial component ρ . We convert this problem into

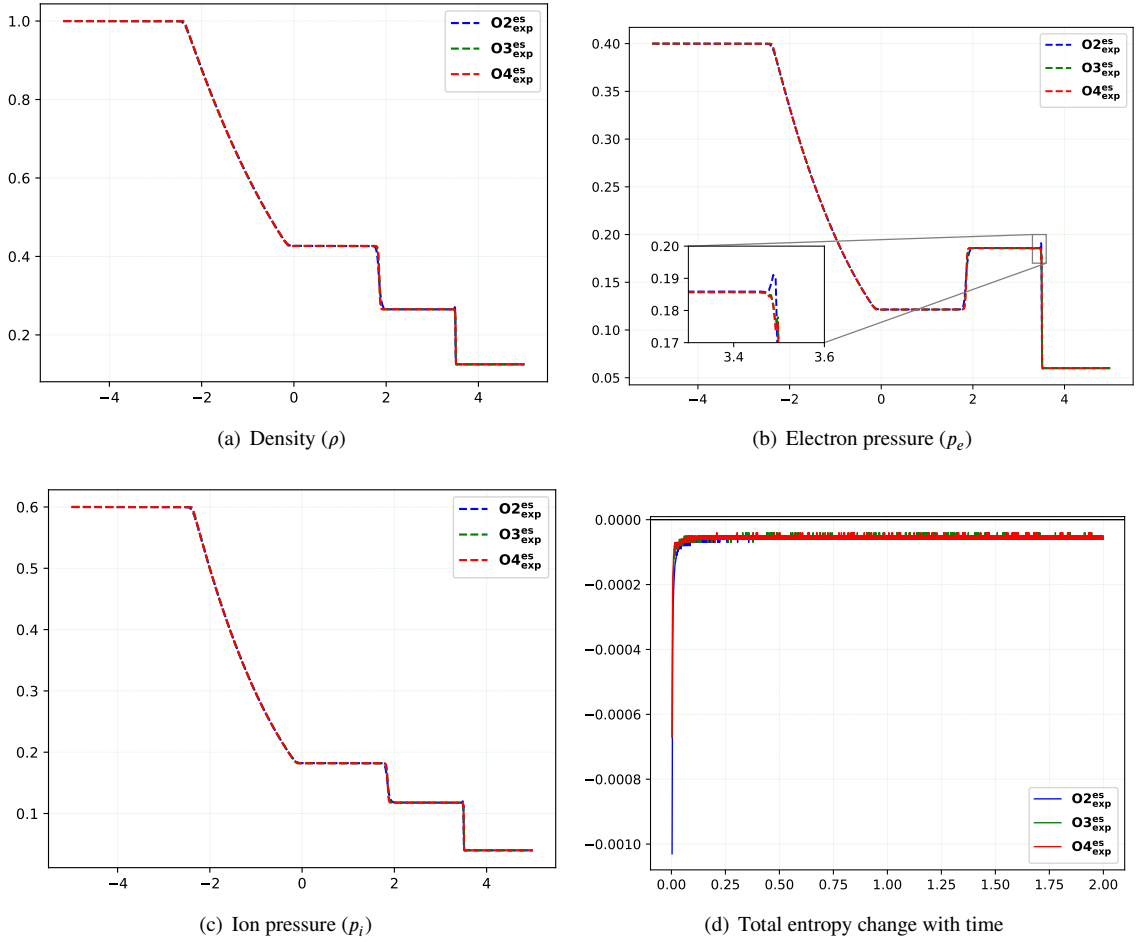


Figure 2: Sod Riemann problem: Plots of density, electron pressure, and ion pressure at $t = 2.0$ using 2000 cells. We have also plotted total entropy change with time.

a two-dimensional test problem. The problem is initialized as follows:

$$\begin{aligned} \rho(x, y, 0) &= 1 + 0.2 \sin(x + y), \\ (\mathbf{v}, p_e, p_i) &= (0.5, 0.5, 2, 2). \end{aligned}$$

with $\gamma_e = \gamma_i = 1.4$. We use periodic boundary conditions on the domain $(x, y) \in [0, 2\pi] \times [0, 2\pi]$. For this setup, the exact solution is $\rho(x, t) = 1 + 0.2 \sin(x + y - t)$. Table(5) presents the L_1 -errors of density for the $\mathbf{O2}_{\text{exp}}^{\text{es}}$, $\mathbf{O3}_{\text{exp}}^{\text{es}}$ and $\mathbf{O4}_{\text{exp}}^{\text{es}}$ schemes at time $t = 1.3$. We observe that each scheme achieves the expected order of accuracy.

6.7. Two-dimensional Riemann problem

In this test case, we consider a two-dimensional Riemann problem from [13], which is motivated from the similar problem for the Euler equation of compressible flow in [53, 54]. We consider a computational domain of $[0, 1] \times [0, 1]$ with Neumann boundary conditions. The initial conditions are given by,

$$(\rho, \mathbf{v}, p_e, p_i) = \begin{cases} (1.5, 0, 0, 0.75, 0.75), & \text{if } x > 0.8, y > 0.8 \\ (0.5323, 1.206, 0, 0.15, 0.15), & \text{if } x < 0.8, y > 0.8 \\ (0.138, 1.206, 1.206, 0.0145, 0.0145), & \text{if } x < 0.8, y < 0.8 \\ (0.5323, 0, 1.206, 0.15, 0.15), & \text{if } x > 0.8, y < 0.8 \end{cases}$$

Entropy stable numerical schemes for OFTT-Euler system

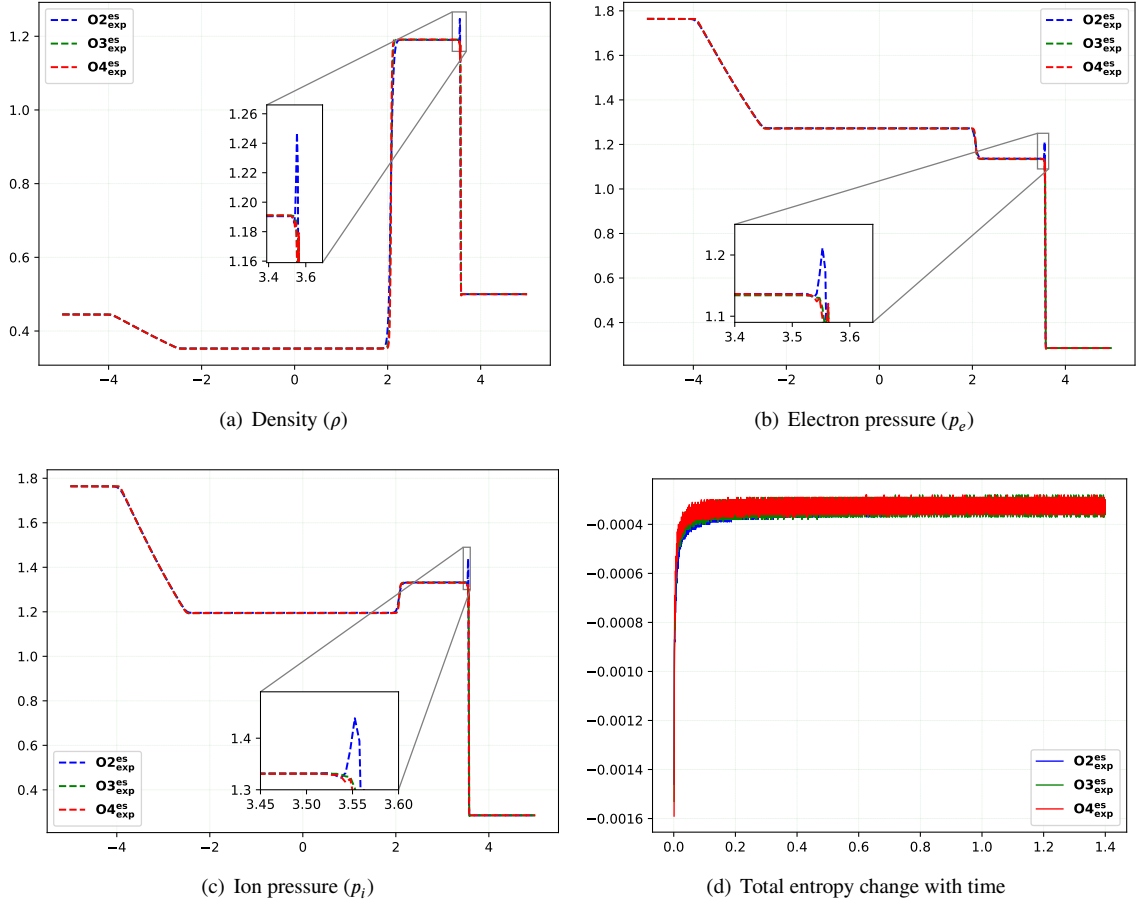


Figure 3: Lax Riemann problem: Plots of density, electron pressure, and ion pressure at $t = 2.0$ using 2000 cells. We have also plotted total entropy change with time.

Table 5
Two-dimensional accuracy test: L_1 errors and order of accuracy for ρ .

Number of cells	$O2_{exp}^{es}$		$O3_{exp}^{es}$		$O4_{exp}^{es}$	
	L_1 error	Order	L_1 error	Order	L_1 error	Order
24×24	1.26E-02	–	7.00E-04	–	1.60E-04	–
48×48	5.03E-03	1.318732756	8.86E-05	2.982213119	1.22E-05	3.714219366
96×96	1.45E-03	1.791429385	1.11E-05	2.996847801	8.72E-07	3.801274782
192×192	3.97E-04	1.873327563	1.39E-06	2.998557202	6.01E-08	3.860152037
384×384	1.08E-04	1.874857877	1.74E-07	2.999868426	4.02E-09	3.900473544

Similar to [13], we consider two cases, with different values of gas constants. In the first case, we take $\gamma_e = \gamma_i = 1.4$, and in second case, we take $\gamma_e = 1.4, \gamma_i = 1.67$. Due to the highly nonlinear interaction of different waves, the solutions contain highly complicated multi-scale structures. We compute the results using 400×400 cells.

The numerical results for the first case ($\gamma_e = \gamma_i = 1.4$) are presented in Figures (4) at final time $t = 0.75$, where we have plots of density, electron pressure, and ion pressure for all three schemes. We observe the $O3_{exp}^{es}$ and $O4_{exp}^{es}$ schemes result in a much more detailed solution than the $O2_{exp}^{es}$ scheme.

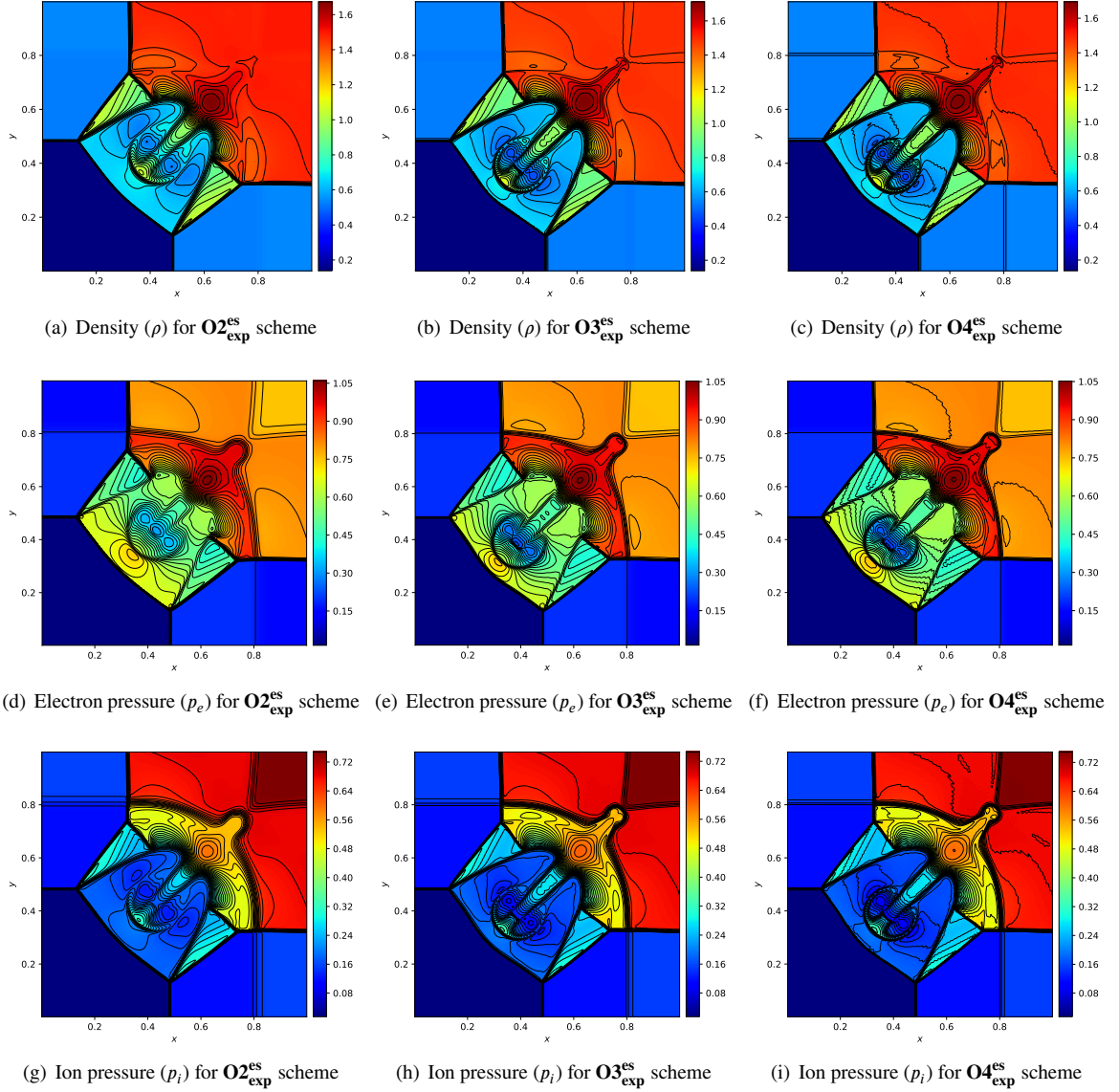


Figure 4: Two-dimensional Riemann problem: Plots of density, electron pressure, and ion pressure at time $t = 0.75$ using 400×400 cells for $\gamma_e = \gamma_i = 1.4$.

In Figure (5), we have presented the numerical results for the second case ($\gamma_e = 1.4$, $\gamma_i = 1.67$) at time $t = 0.59$ on 400×400 cells. We have plotted the density, electron pressure, and ion pressure for all three schemes. We note that the solution structure has changed significantly. Numerically, we observe that $\mathbf{O2}_{\text{exp}}^{\text{es}}$ is much more diffusive than the $\mathbf{O3}_{\text{exp}}^{\text{es}}$ and $\mathbf{O4}_{\text{exp}}^{\text{es}}$ schemes.

Total entropy change with time for both cases is plotted in Figure (6). We again see that in both cases $\mathbf{O2}_{\text{exp}}^{\text{es}}$ is more diffusive than $\mathbf{O3}_{\text{exp}}^{\text{es}}$ and $\mathbf{O4}_{\text{exp}}^{\text{es}}$, which are both comparable.

6.8. Shock-bubble interaction problem

Following [16], we consider the shock bubble interaction problem for this test. We consider a computational domain of $[0, 6.5] \times [0, 0.89]$. The initial bubble has its centre at $(3.5, 0)$ with a radius of 0.5, and the internal initial state is

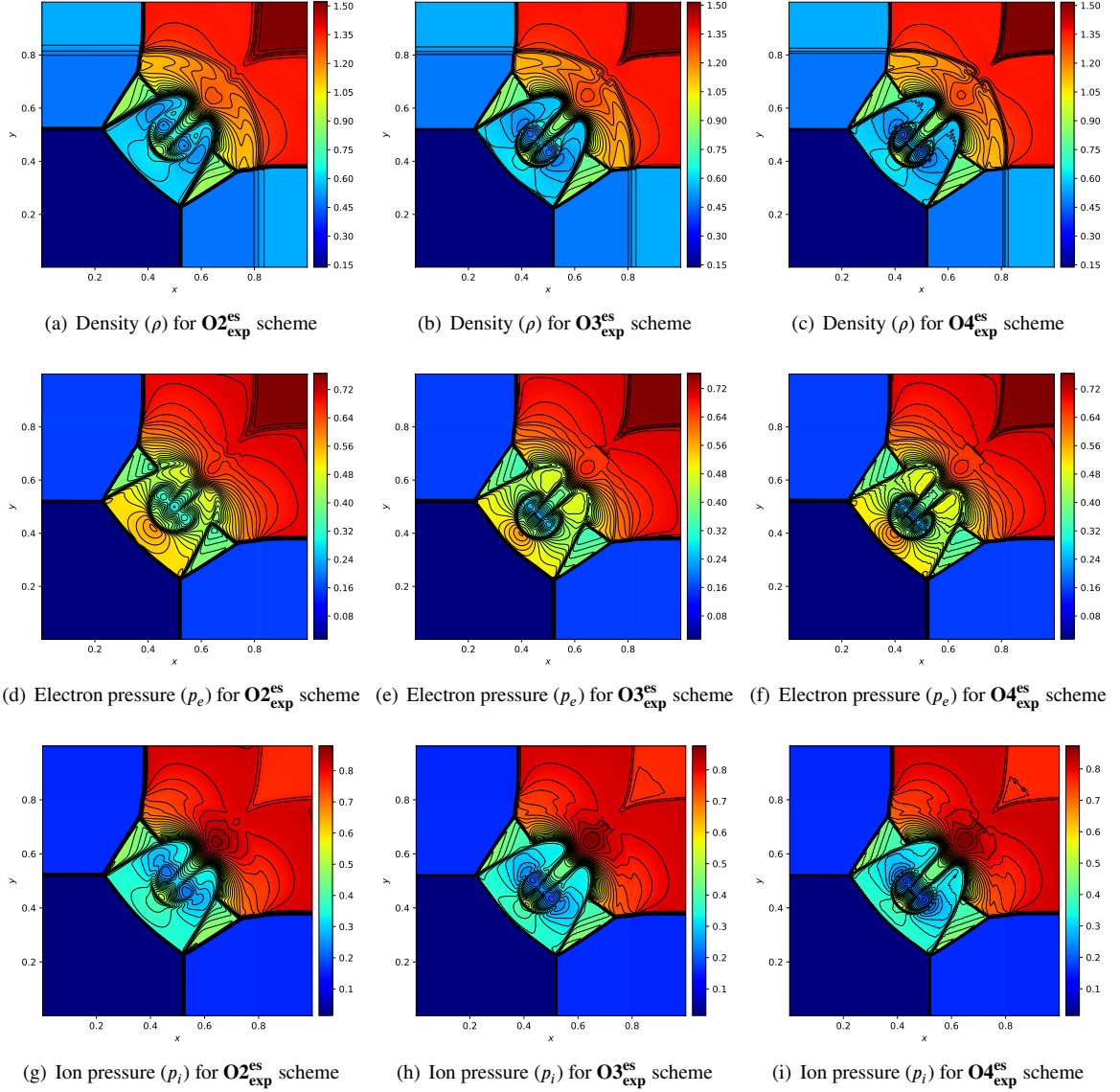


Figure 5: Two-dimensional Riemann problem: Plots of density, electron pressure, and ion pressure at time $t = 0.59$ using 400×400 cells for $\gamma_e = 1.4$, $\gamma_i = 1.67$.

given by,

$$(\rho, \mathbf{v}, p_e, p_i) = (0.1819, 0, 0, 0.220458, 0.220458)$$

In the rest of the domain, we consider the states,

$$(\rho, \mathbf{v}, p_e, p_i) = \begin{cases} (1, 0, 0, 0.3571425, 0.3571425), & \text{if } 0 \leq x < 4.5 \\ (1.3764, -0.3336, 0, 0.560643, 0.560643), & \text{if } 4.5 \leq x < 6.5. \end{cases}$$

The gas constants are $\gamma_e = \gamma_i = 1.4$. We use reflective boundary conditions at the bottom and top boundaries, whereas Dirichlet boundary conditions are used on the left and right boundaries of the domain.

In Figure (7), we have plotted the density for $\mathbf{O2}_{\text{exp}}^{\text{es}}$, $\mathbf{O3}_{\text{exp}}^{\text{es}}$ and $\mathbf{O4}_{\text{exp}}^{\text{es}}$ schemes at time $t = 7.1571$ using 400×144 cells. We observe that the $\mathbf{O2}_{\text{exp}}^{\text{es}}$ scheme is the most diffusive and thus fails to capture small-scale structures effectively.

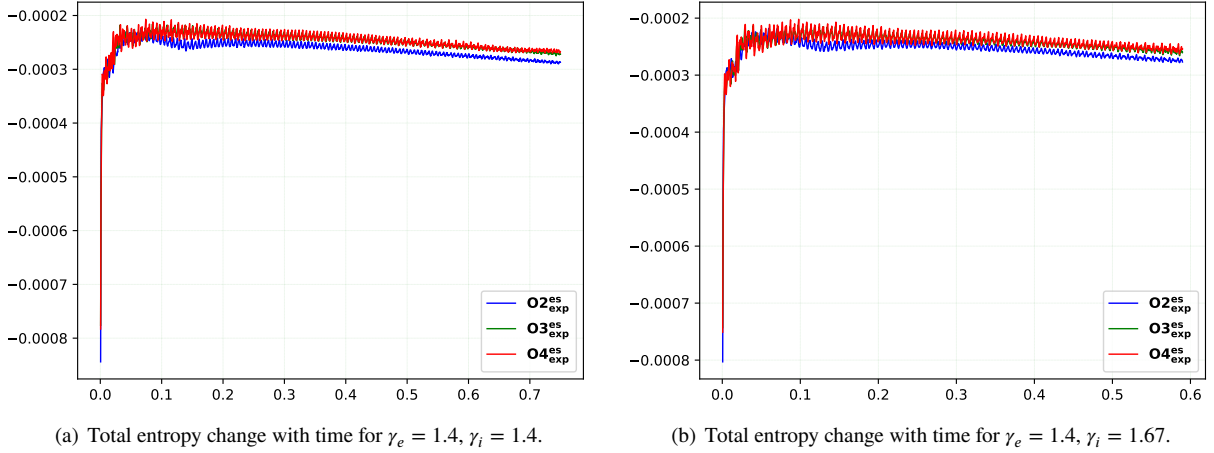


Figure 6: Two-dimensional Riemann problem: Plots of total entropy change with time using 400×400 cells for both the cases using $\mathbf{O2}_{\text{exp}}^{\text{es}}$, $\mathbf{O3}_{\text{exp}}^{\text{es}}$ and $\mathbf{O4}_{\text{exp}}^{\text{es}}$ schemes.

In contrast, the $\mathbf{O4}_{\text{exp}}^{\text{es}}$ scheme is more accurate than the $\mathbf{O3}_{\text{exp}}^{\text{es}}$ scheme, and both are able to capture small-scale structures effectively. We have also plotted the total entropy change with time for all the schemes. We note that all the schemes are entropy stable. Again, we note the diffusive behavior of $\mathbf{O2}_{\text{exp}}^{\text{es}}$ when compared with higher-order schemes $\mathbf{O3}_{\text{exp}}^{\text{es}}$ and $\mathbf{O4}_{\text{exp}}^{\text{es}}$.

In Figure (8), we have also plotted the density at different times $t = 0.6294, 1.1099, 3.3408, 5.0358, 7.1571$, for $\mathbf{O4}_{\text{exp}}^{\text{es}}$ scheme. These simulations illustrate the evolution of the bubble after the shock interaction, its deformation, and finally generate a vortex ring.

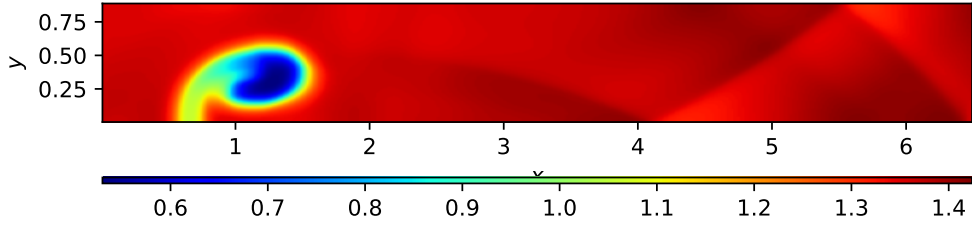
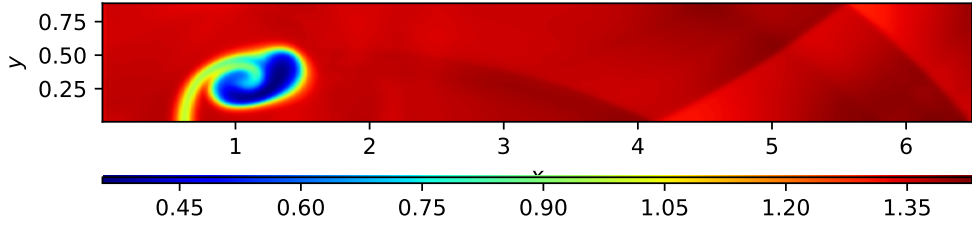
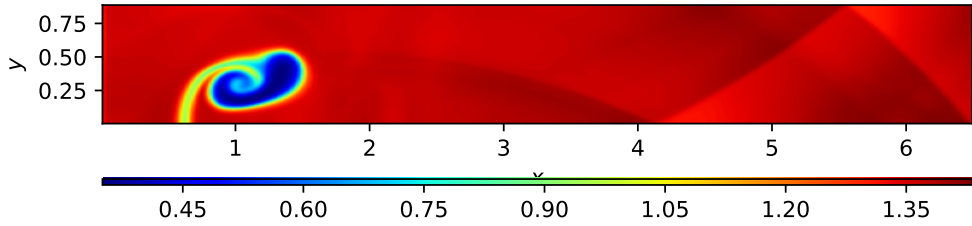
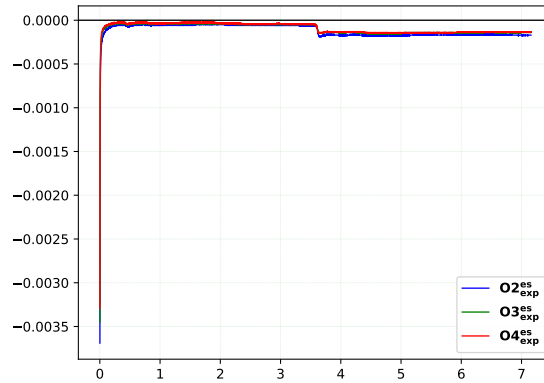
6.9. Richtmyer-Meshkov instability

In the final test case, we consider the Richtmyer-Meshkov instability problem for the OFTT-Euler system proposed in [13], which has applications in ICF (see [55, 56]). We consider a computational domain of $[-12, 12] \times [-12, 12]$. The incident shock wave is initially located at $r_s = 7.5$ and the perturbed contact discontinuity is initially located at $r_c = r_0 + A_0 \cos(\omega\theta)$, where $r_0 = 7.162$, the perturbation amplitude $A_0 = 0.24$, and the perturbation wave number $\omega = 12$. The hydrodynamic instability is caused by the incident shock wave hitting the perturbed contact discontinuity. Following [13], the problem is initialized as follows:

$$(\rho, \mathbf{v}, p_e, p_i) = \begin{cases} (5.04, 0, 0, 0.6, 0.4), & \text{if } x^2 + y^2 < r_c^2, \\ (1, 0, 0, 0.6, 0.4), & \text{if } r_c^2 < x^2 + y^2 < r_s^2, \\ (1.479, -0.518 \cos(\theta), -0.518 \sin(\theta), 1.041, 0.788), & \text{otherwise,} \end{cases}$$

with $\gamma_e = 1.4$ and $\gamma_i = 1.67$. We use Neumann boundary conditions.

We have presented numerical results in Figure (9) for the $\mathbf{O2}_{\text{exp}}^{\text{es}}$, $\mathbf{O3}_{\text{exp}}^{\text{es}}$ and $\mathbf{O4}_{\text{exp}}^{\text{es}}$ schemes at time $t = 17.46$ using 800×800 cells. We have plotted density, electron pressure, and ion pressure. We observe that $\mathbf{O2}_{\text{exp}}^{\text{es}}$ is the most diffusive and fails to capture small-scale structures effectively. Whereas the higher-order schemes $\mathbf{O3}_{\text{exp}}^{\text{es}}$ and $\mathbf{O4}_{\text{exp}}^{\text{es}}$ are much more accurate and able to capture the small-scale features. To demonstrate this, we have also plotted the zoomed-in plots of the results in Figure (10), where we have zoomed at the center of the domain. We clearly see that $\mathbf{O3}_{\text{exp}}^{\text{es}}$ and $\mathbf{O4}_{\text{exp}}^{\text{es}}$ schemes produce lot more details of small-scale structures than the $\mathbf{O2}_{\text{exp}}^{\text{es}}$ scheme. The results are also similar to those presented in [13]. In Figure (11), we have plotted the total entropy change with time. The plot clearly demonstrates the entropy stability of the numerical schemes.


 (a) Density (ρ) for $O2_{\text{exp}}^{\text{es}}$ scheme

 (b) Density (ρ) for $O3_{\text{exp}}^{\text{es}}$ scheme

 (c) Density (ρ) for $O4_{\text{exp}}^{\text{es}}$ scheme


(d) Total entropy change with time

Figure 7: Shock-bubble interaction problem: Plots of density and total entropy evolution at time $t = 7.1571$ using 400×144 cells. We have also plotted the total entropy change with time.

7. Conclusion

In this work, we have designed higher-order entropy-stable finite difference schemes for the One-Fluid Two-Temperature Euler Non-equilibrium Hydrodynamics system, which are a set of hyperbolic PDEs with non-conservative terms. We show that the presence of the non-conservative terms results in non-symmetrizability of the systems. To design entropy-stable numerical schemes, we present a novel reformulation of the equations so that the conservative

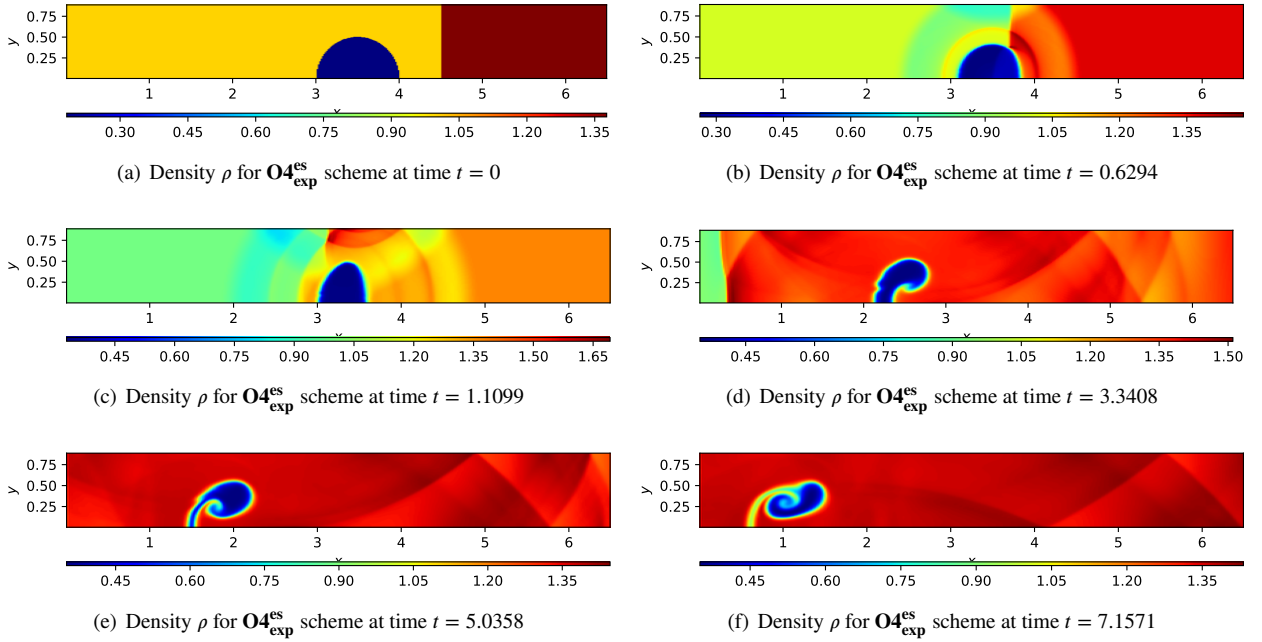


Figure 8: Shock-bubble interaction problem: Plots of density for $\mathbf{O4}_{\text{exp}}^{\text{es}}$ scheme using 400×144 cells at different times.

part is symmetrizable and the non-conservative part does not contribute to the entropy evolution. Finally, an entropy-stable discretization for the new conservative part is proposed, which results in the entropy stability of the complete discretization. We have presented extensive numerical results to demonstrate the accuracy and entropy stability of the proposed numerical schemes.

Acknowledgements

Harish Kumar acknowledge support from a Vajra award (VJR/2018/00129).

CRedit authorship contribution statement

Chetan Singh: Formal analysis, Investigation, Methodology, Software, Visualization, Validation, Conceptualization, Writing – original draft. **Harish Kumar:** Conceptualization, Supervision, Writing – original draft, Writing – review & editing, Funding acquisition .

Declarations

Conflict of interest The authors declare that they have no Conflict of interest.

Data availability

Data will be made available on request.

References

- [1] John I Castor. Astrophysical radiation dynamics: The prospects for scaling. *Astrophysics and Space Science*, 307(1):207–211, 2007.
- [2] Volker Springel. Smoothed particle hydrodynamics in astrophysics. *Annual Review of Astronomy and Astrophysics*, 48:391–430, 2010.
- [3] Romain Teyssier. Grid-based hydrodynamics in astrophysical fluid flows. *Annual Review of Astronomy and Astrophysics*, 53(1):325–364, 2015.

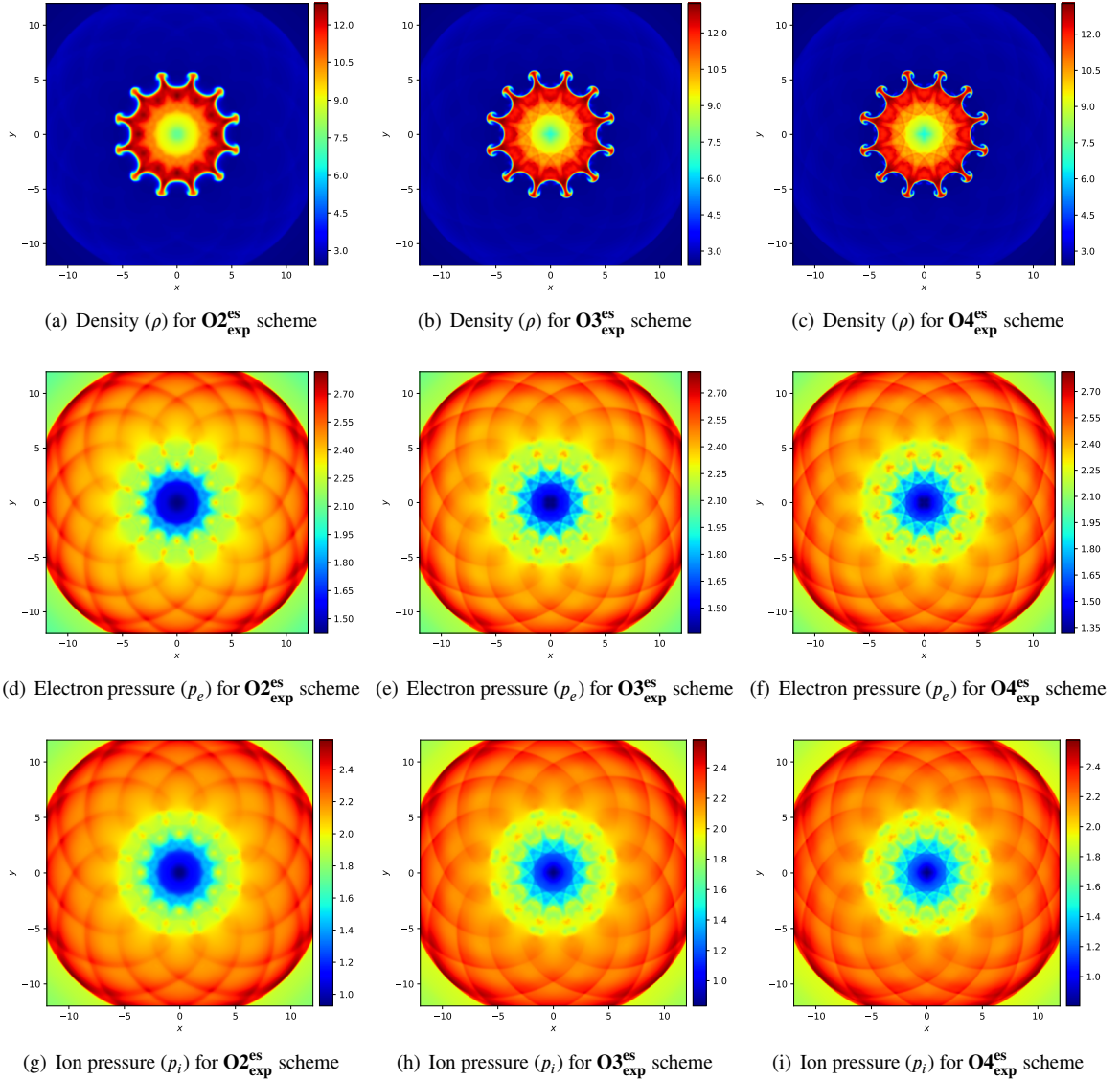


Figure 9: Richtmyer-Meshkov instability: Plots of density, electron pressure and ion pressure at time $t = 17.46$ using 800×800 cells.

- [4] Karl-Heinz A Winkler and Michael L Norman. *Astrophysical radiation hydrodynamics*, volume 188. Springer Science & Business Media, 2012.
- [5] Stefano Atzeni and Jürgen Meyer-ter Vehn. *The Physics of Inertial Fusion: BeamPlasma Interaction, Hydrodynamics, Hot Dense Matter*. Number 125. Oxford University Press, 2004.
- [6] R Paul Drake. Radiation hydrodynamics. In *High-Energy-Density Physics: Fundamentals, Inertial Fusion, and Experimental Astrophysics*, pages 267–334. Springer, 2006.
- [7] Dimitri Mihalas and Barbara Weibel Mihalas. *Foundations of radiation hydrodynamics*. Courier Corporation, 2013.
- [8] J Sanz, R Betti, VA Smalyuk, M Olazabal-Loume, V Drean, V Tikhonchuk, X Ribeyre, and J Feugeas. Radiation hydrodynamic theory of double ablation fronts in direct-drive inertial confinement fusion. *Physics of Plasmas*, 16(8), 2009.
- [9] R Paul Drake. Introduction to high-energy-density physics. In *High-Energy-Density Physics: Fundamentals, Inertial Fusion, and Experimental Astrophysics*, pages 1–17. Springer, 2006.
- [10] R Paul Drake. A journey through high-energy-density physics. *Nuclear Fusion*, 59(3):035001, 2018.
- [11] Ronald C Davidson, T Katsouleas, J Arons, M Baring, C Deeney, L Di Mauro, T Ditmire, R Falcone, D Hammer, W Hill, et al. Frontiers for discovery in high energy density physics. Technical report, DOESC (USDOE Office of Science (SC)), 2004.

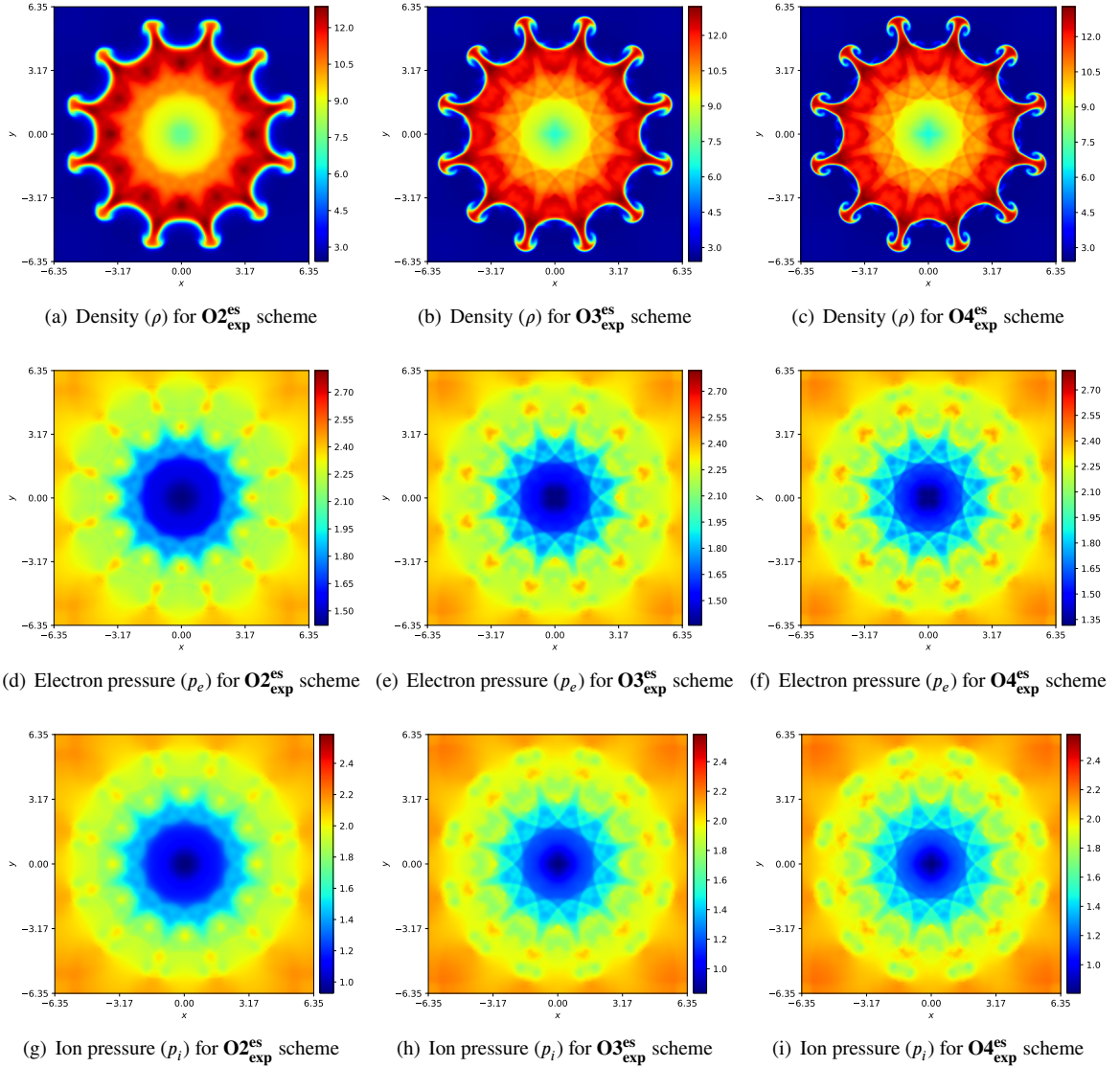


Figure 10: Richtmyer-Meshkov instability: Zoomed plots of density, electron pressure and ion pressure at time $t = 17.46$ using 800×800 cells.

- [12] M Keith Matzen, MA Sweeney, RG Adams, JR Asay, JE Bailey, GR Bennett, DE Bliss, DD Bloomquist, TA Brunner, RB e Campbell, et al. Pulsed-power-driven high energy density physics and inertial confinement fusion research. *Physics of Plasmas*, 12(5), 2005.
- [13] Jian Cheng. A high-order discontinuous galerkin method for one-fluid two-temperature euler non-equilibrium hydrodynamics. *Journal of Scientific Computing*, 100(3):82, 2024.
- [14] Gianni Dal Maso, Philippe G Lefloch, and François Murat. Definition and weak stability of nonconservative products. *Journal de mathématiques pures et appliquées*, 74(6):483–548, 1995.
- [15] Rémi Abgrall and Smadar Karni. A comment on the computation of non-conservative products. *Journal of Computational Physics*, 229(8):2759–2763, 2010.
- [16] Juan Cheng and Chi-Wang Shu. High order conservative finite difference weno scheme for three-temperature radiation hydrodynamics. *Journal of Computational Physics*, 517:113304, 2024.
- [17] Juan Cheng, Nuo Lei, and Chi-Wang Shu. High order conservative lagrangian scheme for three-temperature radiation hydrodynamics. *Journal of Computational Physics*, 496:112595, 2024.
- [18] Chetan Singh, Deepak Bhojriya, Anshu Yadav, Harish Kumar, and Dinshaw S Balsara. Chew, goldberger & low equations: Eigensystem analysis and applications to one-dimensional test problems. *Computers & Mathematics with Applications*, 188:195–220, 2025.

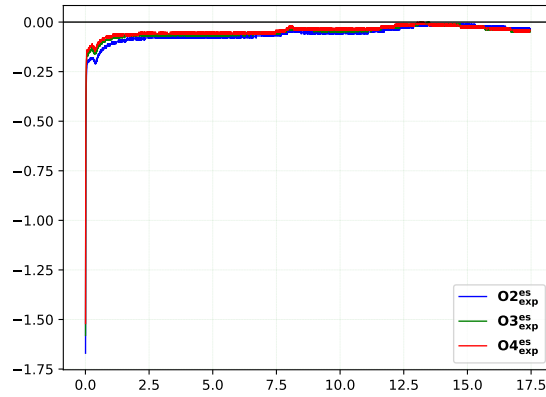


Figure 11: Richtmyer-Meshkov instability: Plots of total entropy change with time using 800×800 cells for $O2_{\text{exp}}^{\text{es}}$, $O3_{\text{exp}}^{\text{es}}$ and $O4_{\text{exp}}^{\text{es}}$ schemes.

- [19] Dinshaw S Balsara, Deepak Bhoriya, Chetan Singh, Harish Kumar, Roger Käppeli, and Federico Gatti. Physical constraint preserving higher-order finite volume schemes for divergence-free astrophysical mhd and rmhd. *The Astrophysical Journal*, 988(1):134, 2025.
- [20] Bruno Després. Lagrangian systems of conservation laws and approximate riemann solvers. In *Godunov Methods: Theory and Applications*, pages 233–245. Springer, 2001.
- [21] Jérôme Breil, Stéphane Galera, and Pierre-Henri Maire. Multi-material ale computation in inertial confinement fusion code chic. *Computers & fluids*, 46(1):161–167, 2011.
- [22] N Ya Moiseev and EA Shestakov. Solution of the riemann problem in twoand three-temperature gas dynamics. *Computational Mathematics and Mathematical Physics*, 55(9):1547–1553, 2015.
- [23] Takashi Shiroto, Soshi Kawai, and Naofumi Ohnishi. Structure-preserving operators for thermal-nonequilibrium hydrodynamics. *Journal of Computational Physics*, 364:1–17, 2018.
- [24] Denise Aregba-Driollet, Jérôme Breil, Stéphane Brull, Bruno Dubroca, and Elise Estibals. Modelling and numerical approximation for the nonconservative bitemperature euler model. *ESAIM: Mathematical Modelling and Numerical Analysis*, 52(4):1353–1383, 2018.
- [25] Christophe Chalons and Frédéric Coquel. The riemann problem for the multi-pressure euler system. *Journal of Hyperbolic Differential Equations*, 2(03):745–782, 2005.
- [26] Guang Lin and George Em Karniadakis. A discontinuous galerkin method for two-temperature plasmas. *Computer methods in applied mechanics and engineering*, 195(25-28):3504–3527, 2006.
- [27] Bernardo Cockburn and Chi-Wang Shu. Tvb runge-kutta local projection discontinuous galerkin finite element method for conservation laws. ii. general framework. *Mathematics of computation*, 52(186):411–435, 1989.
- [28] Bernardo Cockburn and Chi-Wang Shu. The runge–kutta discontinuous galerkin method for conservation laws v: multidimensional systems. *Journal of computational physics*, 141(2):199–224, 1998.
- [29] Afeintou Sangam, Élise Estibals, and Hervé Guillard. Derivation and numerical approximation of two-temperature euler plasma model. *Journal of Computational Physics*, 444:110565, 2021.
- [30] Jian Cheng and Fan Zhang. Mathematical model and numerical discretization for the simulation of two-material two-temperature compressible flows. *Journal of Computational Physics*, 529:113896, 2025.
- [31] Ya-Ru Zhao, Zhen Gao, and Bao-Shan Wang. Fifth-order equilibrium-preserving path-conservative characteristic-wise aweno scheme for one-fluid two-temperature euler model. *Journal of Computational Physics*, page 114409, 2025.
- [32] Jian Cheng and Fan Zhang. Analysis and design of positivity-preserving high-order discontinuous galerkin methods for two-temperature compressible flows. *Journal of Computational Physics*, page 114581, 2025.
- [33] Deepak Bhoriya, Harish Kumar, and Praveen Chandrashekar. High-order finite-difference entropy stable schemes for two-fluid relativistic plasma flow equations. *Journal of Computational Physics*, page 112207, 2023.
- [34] Harish Kumar and Siddhartha Mishra. Entropy Stable Numerical Schemes for Two-Fluid Plasma Equations. *Journal of Scientific Computing*, 52(2):401–425, August 2012.
- [35] Chhanda Sen and Harish Kumar. Entropy Stable Schemes For Ten-Moment Gaussian Closure Equations. *Journal of Scientific Computing*, 75(2):1128–1155, May 2018.
- [36] Praveen Chandrashekar and Christian Klingenberg. Entropy stable finite volume scheme for ideal compressible mhd on 2-d cartesian meshes. *SIAM Journal on Numerical Analysis*, 54(2):1313–1340, 2016.
- [37] Praveen Chandrashekar. Kinetic energy preserving and entropy stable finite volume schemes for compressible euler and navier-stokes equations. *Communications in Computational Physics*, 14(5):1252–1286, 2013.
- [38] Ulrik S Fjordholm, Siddhartha Mishra, and Eitan Tadmor. Arbitrarily high-order accurate entropy stable essentially nonoscillatory schemes for systems of conservation laws. *SIAM Journal on Numerical Analysis*, 50(2):544–573, 2012.

- [39] Eitan Tadmor. Entropy stability theory for difference approximations of nonlinear conservation laws and related time-dependent problems. *Acta Numerica*, 12:451–512, 2003.
- [40] Dominik Derigs, Andrew R Winters, Gregor J Gassner, Stefanie Walch, and Marvin Bohm. Ideal glm-mhd: about the entropy consistent nine-wave magnetic field divergence diminishing ideal magnetohydrodynamics equations. *Journal of Computational Physics*, 364:420–467, 2018.
- [41] Anshu Yadav, Deepak Bhooriya, Harish Kumar, and Praveen Chandrashekar. Entropy stable schemes for the shear shallow water model equations. *Journal of Scientific Computing*, 97(3):77, 2023.
- [42] Chetan Singh, Anshu Yadav, Deepak Bhooriya, Harish Kumar, and Dinshaw S Balsara. Entropy stable finite difference schemes for chew, goldberger and low anisotropic plasma flow equations. *Journal of Scientific Computing*, 102(2):51, 2025.
- [43] Chetan Singh, Harish Kumar, Deepak Bhooriya, and Dinshaw S Balsara. Entropy stable numerical schemes for divergence diminishing chew, goldberger & low equations for plasma flows. *arXiv preprint arXiv:2602.20757*, 2026.
- [44] Andrés M Rueda-Ramírez, Aleksey Sikstel, and Gregor J Gassner. An entropy-stable discontinuous galerkin discretization of the ideal multi-ion magnetohydrodynamics system. *arXiv preprint arXiv:2402.14615*, 2024.
- [45] Eitan Tadmor. The numerical viscosity of entropy stable schemes for systems of conservation laws. i. *Mathematics of Computation*, 49(179):91–103, 1987.
- [46] Philip L Roe. Affordable, entropy consistent flux functions. In *Eleventh International Conference on Hyperbolic Problems: Theory, Numerics and Applications*, Lyon, 2006.
- [47] Farzad Ismail and Philip L Roe. Affordable, entropy-consistent euler flux functions ii: Entropy production at shocks. *Journal of Computational Physics*, 228(15):5410–5436, 2009.
- [48] Philippe G Lefloch, Jean-Marc Mercier, and Christian Rohde. Fully discrete, entropy conservative schemes of arbitrary order. *SIAM Journal on Numerical Analysis*, 40(5):1968–1992, 2002.
- [49] Timothy J Barth. Numerical methods for gasdynamic systems on unstructured meshes. *An Introduction to Recent Developments in Theory and Numerics for Conservation Laws: Proceedings of the International School on Theory and Numerics for Conservation Laws, Freiburg/Littenweiler, October 20–24, 1997*, pages 195–285, 1999.
- [50] Ulrik S Fjordholm, Siddhartha Mishra, and Eitan Tadmor. Eno reconstruction and eno interpolation are stable. *Foundations of Computational Mathematics*, 13(2):139–159, 2013.
- [51] Sigal Gottlieb, Chi-Wang Shu, and Eitan Tadmor. Strong stability-preserving high-order time discretization methods. *SIAM review*, 43(1):89–112, 2001.
- [52] Yong Liu, Jianfang Lu, and Chi-Wang Shu. An entropy stable essentially oscillation-free discontinuous galerkin method for solving ideal magnetohydrodynamic equations. *Journal of Computational Physics*, 530:113911, 2025.
- [53] Peter D Lax and Xu-Dong Liu. Solution of two-dimensional riemann problems of gas dynamics by positive schemes. *SIAM Journal on Scientific Computing*, 19(2):319–340, 1998.
- [54] Liang Pan, Jiequan Li, and Kun Xu. A few benchmark test cases for higher-order euler solvers. *Numerical Mathematics: Theory, Methods and Applications*, 10(4):711–736, 2017.
- [55] Baolin Tian, Dexun Fu, and Yanwen Ma. Numerical investigation of richtmyer-meshkov instability driven by cylindrical shocks. *Acta Mechanica Sinica*, 22(1):9–16, 2006.
- [56] Joshua Paul Sauppe, Sasikumar Palaniyappan, Eric Nicholas Loomis, John L Kline, Kirk Adler Flippo, and Bhuvana Srinivasan. Using cylindrical implsions to investigate hydrodynamic instabilities in convergent geometry. *Matter and Radiation at Extremes*, 4(6), 2019.
- [57] Edwige Godlewski and Pierre-Arnaud Raviart. *Numerical approximation of hyperbolic systems of conservation laws*, volume 118. Springer Science & Business Media, 2013.

A. Entropy invariance of non-conservative terms in reformulated OFTT-Euler system

Lemma A.1. *The non-conservative terms of the reformulated system (12) do not contribute to the entropy evolution, i.e., the coefficient matrices $\mathbf{C}_x(\mathbf{U})$ and $\mathbf{C}_y(\mathbf{U})$ satisfy,*

$$\mathbf{v}^\top \mathbf{C}_x(\mathbf{U}) = \mathbf{v}^\top \mathbf{C}_y(\mathbf{U}) = 0.$$

Proof. We compute $\mathbf{v}^\top \cdot \mathbf{C}_i$ for $i = \{1, 2, 3, 4, 5\}$, where \mathbf{C}_i are the columns of the matrix $\mathbf{C}_x(\mathbf{U})$. We get,

$$\begin{aligned} \mathbf{v}^\top \cdot \mathbf{C}_1 &= \mathbf{v}^\top \cdot \left\{ 0, -\frac{(\gamma_e - 1)|\mathbf{v}|^2}{2}, 0, -\left(\frac{(\gamma_e - 1)|\mathbf{v}|^2}{2} + \frac{p_i - p_e}{\rho}\right)v_x, -\frac{(\gamma_i - 1)p_i v_x}{\rho} \right\} \\ &= -\frac{(\gamma_e - 1)|\mathbf{v}|^2}{2} (\beta_e v_x) - \left(\frac{(\gamma_e - 1)|\mathbf{v}|^2}{2} + \frac{p_i - p_e}{\rho}\right)v_x (-\beta_e) - \frac{(\gamma_i - 1)p_i v_x}{\rho} \left(\frac{\beta_e - \beta_i}{\gamma_i - 1}\right) \\ &= 0, \end{aligned}$$

$$\begin{aligned} \mathbf{v}^\top \cdot \mathbf{C}_2 &= \mathbf{v}^\top \cdot \left\{ 0, (\gamma_e - 1)v_x, 0, (\gamma_e - 1)v_x^2 + \frac{p_i - p_e}{\rho}, \frac{(\gamma_i - 1)p_i}{\rho} \right\} \\ &= (\gamma_e - 1)v_x (\beta_e v_x) + \left(\frac{(\gamma_e - 1)v_x^2 + \frac{p_i - p_e}{\rho}}{\rho}\right) (-\beta_e) + \frac{(\gamma_i - 1)p_i}{\rho} \left(\frac{\beta_e - \beta_i}{\gamma_i - 1}\right) \end{aligned}$$

$$= 0,$$

$$\mathbf{v}^\top \cdot \mathbf{C}_3 = \mathbf{v}^\top \cdot \{0, (\gamma_e - 1)v_y, 0, (\gamma_e - 1)v_x v_y, 0\} = 0,$$

$$\mathbf{v}^\top \cdot \mathbf{C}_4 = \mathbf{v}^\top \cdot \{0, -(\gamma_e - 1), 0, -(\gamma_e - 1)v_x, 0\} = 0,$$

and

$$\mathbf{v}^\top \cdot \mathbf{C}_5 = \mathbf{v}^\top \cdot \left\{ 0, \left(\frac{\gamma_e - 1}{\gamma_i - 1} + 1 \right), 0, \left(\frac{\gamma_e - 1}{\gamma_i - 1} + 1 \right) v_x, 0 \right\} = 0.$$

Hence $\mathbf{v}^\top \mathbf{C}_x(\mathbf{U}) = 0$. Similarly, we can easily prove that $\mathbf{v}^\top \mathbf{C}_y(\mathbf{U}) = 0$. \square

B. Non-symmetrizability of OFTT-Euler system

Here, we investigate symmetrization of the OFTT-Euler system. Let us recall,

Definition B.1. *The conservation law*

$$\frac{\partial \mathbf{U}}{\partial t} + \frac{\partial \mathbf{f}_x}{\partial x} = 0, \quad (34)$$

is said to be symmetrizable if there exists a change of variable $\mathbf{U} \rightarrow \mathbf{V}$ which symmetrizes it, i.e., (34) with a change of variable can be written as,

$$\frac{\partial \mathbf{U}}{\partial \mathbf{V}} \frac{\partial \mathbf{V}}{\partial t} + \frac{\partial \mathbf{f}_x}{\partial \mathbf{U}} \frac{\partial \mathbf{U}}{\partial \mathbf{V}} \frac{\partial \mathbf{V}}{\partial x} = 0.$$

where $\frac{\partial \mathbf{U}}{\partial \mathbf{V}}$ is a symmetric positive definite matrix. Furthermore, $\frac{\partial \mathbf{f}_x}{\partial \mathbf{U}} \frac{\partial \mathbf{U}}{\partial \mathbf{V}}$ is symmetric matrices.

We also have the following results from [57]:

Theorem B.1. *The conservative system have a strictly convex entropy $\mathcal{E}(\mathbf{U})$ if and only if the system is symmetrizable.*

Remark B.1. *The conservative part of the OFTT-Euler system is symmetrizable because it satisfies,*

$$\frac{\partial \mathbf{f}_x}{\partial \mathbf{V}} = \left(\frac{\partial \mathbf{f}_x}{\partial \mathbf{U}} \right)^\top.$$

We now consider the complete OFTT-Euler system in one dimension, i.e.

$$\frac{\partial \mathbf{U}}{\partial t} + \frac{\partial \mathbf{f}_x}{\partial x} + \mathbf{C}_x(\mathbf{U}) \frac{\partial \mathbf{U}}{\partial x} = 0. \quad (35)$$

where \mathbf{U} , \mathbf{f}_x and $\mathbf{C}_x(\mathbf{U})$ are defined in (3.1). Following [41], to prove the symmetrizability of the system, we need to prove that the matrix

$$\mathcal{H}(\mathbf{U}) = \left(\frac{\partial \mathbf{f}_x}{\partial \mathbf{U}} + \mathbf{C}_x(\mathbf{U}) \right) \frac{\partial \mathbf{U}}{\partial \mathbf{V}},$$

is symmetric. However, a lengthy calculation shows that

$$\mathcal{H}(\mathbf{U}) - \mathcal{H}(\mathbf{U})^\top = \begin{pmatrix} 0 & \frac{p_e - p_i}{2} & 0 & \frac{(p_e - p_i)v_x}{2} & 0 \\ \frac{p_i - p_e}{2} & 0 & \frac{(p_i - p_e)v_y}{2} & \Gamma & -\frac{(p_e - p_i)p_i(-1+2\gamma_i)}{2\rho} \\ 0 & \frac{(p_e - p_i)v_y}{2} & 0 & \frac{(p_e - p_i)v_x v_y}{2} & 0 \\ \frac{(p_i - p_e)v_x}{2} & -\Gamma & \frac{(p_i - p_e)v_x v_y}{2} & 0 & -\frac{(p_e - p_i)p_i v_x(-1+2\gamma_i)}{2\rho} \\ 0 & \frac{(p_e - p_i)p_i(-1+2\gamma_i)}{2\rho} & 0 & \frac{(p_e - p_i)p_i v_x(-1+2\gamma_i)}{2\rho} & 0 \end{pmatrix}.$$

with $\Gamma = \frac{(p_e - p_i)(-2p_e(\gamma_i - 1) + (\gamma_e - 1)(2p_i(1 - 2\gamma_i) + \rho(v_x^2 - v_y^2)(\gamma_i - 1)))}{4\rho(\gamma_e - 1)(\gamma_i - 1)}$. Which is not zero. Hence, the system is not symmetrizable. However, we note that when $p_e = p_i$ the matrix $\mathcal{H}(\mathbf{U})$ is symmetric, which is expected as in that case, the OFTT-Euler system reduces to compressible Euler equations.

C. Entropy-scaled right eigenvectors for conservative part of the reformulated OFTT-Euler system

We consider the conservative part of the OFTT-Euler system

$$\frac{\partial \mathbf{U}}{\partial t} + \sum_{d \in \{x,y\}} \frac{\partial \mathbf{f}_d}{\partial \mathbf{U}} \frac{\partial \mathbf{U}}{\partial d} = 0. \quad (36)$$

Let us consider the primitive variables $\mathbf{W} = \{\rho, v_x, v_y, p_e, p_i\}$. For system (36), Section (C.1) describes the right eigenvectors with respect to the primitive variables, while Section (C.3) shows the expressions for the scaled eigenvectors with respect to the primitive variables.

C.1. Right eigenvectors

To compute eigenstructure, we rewrite (36) in terms of primitive variables \mathbf{W} . The eigenvalues $\tilde{\Lambda}_d$ of the Jacobian $\frac{\partial \mathbf{f}_d}{\partial \mathbf{U}}$ are then

$$\tilde{\Lambda}_d = (v_d, v_d, v_d, v_d \pm c_f), \quad \text{where } c_f = \sqrt{\frac{2p_e(2\gamma_e - 1)}{\rho}}$$

The corresponding right eigenvectors corresponding to eigenvalues $v_x, v_x, v_x, v_x \pm c_f$ are given below,

$$\begin{pmatrix} 1 \\ 0 \\ 0 \\ 0 \\ 0 \end{pmatrix}, \begin{pmatrix} 0 \\ 0 \\ 1 \\ 0 \\ 0 \end{pmatrix}, \begin{pmatrix} 0 \\ 0 \\ 0 \\ 0 \\ 1 \end{pmatrix}, \begin{pmatrix} \rho^2 \\ \pm \sqrt{2p_e(2\gamma_e - 1)\rho} \\ 0 \\ p_e(2\gamma_e - 1)\rho \\ p_i\rho \end{pmatrix}.$$

Similarly, the corresponding right eigenvectors corresponding to eigenvalues $v_y, v_y, v_y, v_y \pm c_f$ are given below,

$$\begin{pmatrix} 1 \\ 0 \\ 0 \\ 0 \\ 0 \end{pmatrix}, \begin{pmatrix} 0 \\ 1 \\ 0 \\ 0 \\ 0 \end{pmatrix}, \begin{pmatrix} 0 \\ 0 \\ 0 \\ 0 \\ 1 \end{pmatrix}, \begin{pmatrix} \rho^2 \\ 0 \\ \pm \sqrt{2p_e(2\gamma_e - 1)\rho} \\ p_e(2\gamma_e - 1)\rho \\ p_i\rho \end{pmatrix}.$$

Under the assumption $\gamma_e > 1, \gamma_i > 1$ and equation (5), all eigenvalues are real, and the set of eigenvectors in both directions is linearly independent.

C.2. Entropy scaled right eigenvectors via Barth scaling process

Here, we will compute the entropy-scaled right eigenvectors in x -direction using the Barth scaling procedure [49]. The right eigenvectors of the Jacobian matrix $\frac{\partial \mathbf{f}_x}{\partial \mathbf{U}}$ for the system (36) are described in C.1 in terms of primitive variables. Next, we define

$$R^x = \frac{\partial \mathbf{U}}{\partial \mathbf{W}} R_{\mathbf{W}}^x,$$

where R^x is the right eigenvector matrix for the Jacobian matrix $\frac{\partial \mathbf{f}_x}{\partial \mathbf{U}}$ in terms of conservative variables and $\frac{\partial \mathbf{U}}{\partial \mathbf{W}}$ is the Jacobian matrix for the change of variables, which is given below

$$\frac{\partial \mathbf{U}}{\partial \mathbf{W}} = \begin{pmatrix} 1 & 0 & 0 & 0 & 0 \\ v_x & \rho & 0 & 0 & 0 \\ v_y & 0 & \rho & 0 & 0 \\ \frac{|v|^2}{2} & \rho v_x & \rho v_y & \frac{1}{\gamma_e - 1} & \frac{1}{\gamma_i - 1} \\ 0 & 0 & 0 & 0 & 1 \end{pmatrix}.$$

The matrix $R_{\mathbf{W}}^x$ is the right eigenvector matrix for the Jacobian matrix $\frac{\partial \mathbf{f}_x}{\partial \mathbf{U}}$ in terms of the primitive variable (see C.1), which is given below,

$$\begin{pmatrix} \rho^2 & 1 & 0 & 0 & \rho^2 \\ -\sqrt{2p_e(2\gamma_e-1)}\rho & 0 & 0 & 0 & \sqrt{2p_e(2\gamma_e-1)}\rho \\ 0 & 0 & 1 & 0 & 0 \\ p_e(2\gamma_e-1)\rho & 0 & 0 & 0 & p_e(2\gamma_e-1)\rho \\ p_i\rho & 0 & 0 & 1 & p_i\rho \end{pmatrix}.$$

We want to determine the scaling matrix T^x that will allow the scaled right-eigenvector matrix $\tilde{R}^x = R^x T^x$ to satisfy

$$\frac{\partial \mathbf{U}}{\partial \mathcal{V}} = \tilde{R}^x \tilde{R}^{x\top}, \quad (92)$$

where the entropy variable \mathcal{V} is defined in (13). Now we follow [49] and define the matrix

$$\mathcal{Y}^x = (R_{\mathbf{W}}^x)^{-1} \frac{\partial \mathbf{W}}{\partial \mathcal{V}} \left(\frac{\partial \mathbf{U}}{\partial \mathbf{W}} \right)^{-\top} (R_{\mathbf{W}}^x)^{-\top}.$$

This results in,

$$\mathcal{Y}^x = \begin{pmatrix} \frac{1}{4\rho^3(2\gamma_e-1)} & 0 & 0 & 0 & 0 \\ 0 & \frac{\rho(\gamma_e-1)}{(2\gamma_e-1)} & 0 & \frac{p_i(\gamma_e-1)}{(2\gamma_e-1)} & 0 \\ 0 & 0 & \frac{p_e}{\rho^2} & 0 & 0 \\ 0 & \frac{p_i(\gamma_e-1)}{(2\gamma_e-1)} & 0 & -\frac{p_i^2(\gamma_e+\gamma_i-2\gamma_e\gamma_i)}{\rho(2\gamma_e-1)} & 0 \\ 0 & 0 & 0 & 0 & \frac{1}{4\rho^3(2\gamma_e-1)} \end{pmatrix}.$$

Then the scaling matrix T^x is the square root of \mathcal{Y}^x , which is given by,

$$\begin{pmatrix} \frac{1}{\sqrt{4\rho^3(2\gamma_e-1)}} & 0 & 0 & 0 & 0 \\ 0 & \frac{p_i\Theta_1+\rho(\gamma_e-1)}{(2\gamma_e-1)\Theta} & 0 & \frac{p_i(\gamma_e-1)}{(2\gamma_e-1)\Theta} & 0 \\ 0 & 0 & \frac{\sqrt{p_e}}{\rho} & 0 & 0 \\ 0 & \frac{p_i(\gamma_e-1)}{(2\gamma_e-1)\Theta} & 0 & \frac{p_i^2(-\gamma_i+\gamma_e(2\gamma_i-1))+p_i\rho\Theta_1}{\rho(2\gamma_e-1)\Theta} & 0 \\ 0 & 0 & 0 & 0 & \frac{1}{\sqrt{4\rho^3(2\gamma_e-1)}} \end{pmatrix},$$

where, $\Theta_1 = \sqrt{(\gamma_e-1)(\gamma_i-1)(2\gamma_e-1)}$ and $\Theta = \sqrt{\frac{2p_i\rho\Theta_1-p_i^2(\gamma_e+\gamma_i-2\gamma_e\gamma_i)+\rho^2(\gamma_e-1)}{\rho(2\gamma_e-1)}}$.

Similarly, we can obtain the scaling matrix T^y , which turns out to be same as the matrix T^x .

C.3. Entropy scaled right eigenvectors in x and y direction

Finally, we provide the complete expressions for the entropy-scaled eigenvectors. In the x -direction, the entropy-scaled right eigenvectors matrix in terms of primitive variables is

$$\begin{pmatrix} \sqrt{\frac{\rho}{4(2\gamma_e-1)}} & \frac{p_i\Theta_1+\rho(\gamma_e-1)}{(2\gamma_e-1)\Theta} & 0 & \frac{p_i(\gamma_e-1)}{(2\gamma_e-1)\Theta} & \sqrt{\frac{\rho}{4(2\gamma_e-1)}} \\ -\frac{1}{\rho}\sqrt{\frac{p_e}{2}} & 0 & 0 & 0 & \frac{1}{\rho}\sqrt{\frac{p_e}{2}} \\ 0 & 0 & \frac{\sqrt{p_e}}{\rho} & 0 & 0 \\ \frac{p_e}{2}\sqrt{\frac{(2\gamma_e-1)}{\rho}} & 0 & 0 & 0 & \frac{p_e}{2}\sqrt{\frac{(2\gamma_e-1)}{\rho}} \\ \frac{p_i}{2}\sqrt{\frac{1}{(2\gamma_e-1)\rho}} & \frac{p_i(\gamma_e-1)}{(2\gamma_e-1)\Theta} & 0 & \frac{p_i^2(-\gamma_i+\gamma_e(2\gamma_i-1))+p_i\rho\Theta_1}{\rho(2\gamma_e-1)\Theta} & \frac{p_i}{2}\sqrt{\frac{1}{(2\gamma_e-1)\rho}} \end{pmatrix}.$$

Similarly, in the y -direction, the entropy-scaled right eigenvectors matrix in terms of primitive variables is

$$\begin{pmatrix} \sqrt{\frac{\rho}{4(2\gamma_e-1)}} & \frac{p_i\Theta_1+\rho(\gamma_e-1)}{(2\gamma_e-1)\Theta} & 0 & \frac{p_i(\gamma_e-1)}{(2\gamma_e-1)\Theta} & \sqrt{\frac{\rho}{4(2\gamma_e-1)}} \\ 0 & 0 & \frac{\sqrt{p_e}}{\rho} & 0 & 0 \\ -\frac{1}{\rho}\sqrt{\frac{p_e}{2}} & 0 & 0 & 0 & \frac{1}{\rho}\sqrt{\frac{p_e}{2}} \\ \frac{p_e}{2}\sqrt{\frac{(2\gamma_e-1)}{\rho}} & 0 & 0 & 0 & \frac{p_e}{2}\sqrt{\frac{(2\gamma_e-1)}{\rho}} \\ \frac{p_i}{2}\sqrt{\frac{1}{(2\gamma_e-1)\rho}} & \frac{p_i(\gamma_e-1)}{(2\gamma_e-1)\Theta} & 0 & \frac{p_i^2(-\gamma_i+\gamma_e(2\gamma_i-1))+p_i\rho\Theta_1}{\rho(2\gamma_e-1)\Theta} & \frac{p_i}{2}\sqrt{\frac{1}{(2\gamma_e-1)\rho}} \end{pmatrix}.$$

Where, $\Theta_1 = \sqrt{(\gamma_e - 1)(\gamma_i - 1)(2\gamma_e - 1)}$ and $\Theta = \sqrt{\frac{2p_i\rho\Theta_1 - p_i^2(\gamma_e + \gamma_i - 2\gamma_e\gamma_i) + \rho^2(\gamma_e - 1)}{\rho(2\gamma_e - 1)}}$.